ELSEVIER

J. Non-Newtonian Fluid Mech. xxx (2006) xxx–xxx

Journal of Non-Newtonian Fluid Mechanics

www.elsevier.com/locate/jnnfm

Multiscale simulation of viscoelastic free surface flows

Mohit Bajaj [a], Pradeep P. Bhat [b], J. Ravi Prakash [a], Matteo Pasquali [b,*]

[a] *Department of Chemical Engineering, Monash University, Clayton, Vic. 3800, Australia*
[b] *Department of Chemical and Biomolecular Engineering, MS 362, Rice University, Houston, TX 77005, USA*

Received 24 November 2005; received in revised form 4 April 2006; accepted 24 April 2006

Abstract

A micro–macro approach based on combining the Brownian configuration fields (BCF) method [M.A. Hulsen, A.P.G. van Heel, B.H.A.A. van den Brule, Simulation of viscoelastic flow using Brownian configuration fields, J. Non-Newtonian Fluid Mech. 70 (1997) 79–101] with an Arbitrary Lagrangian–Eulerian (ALE) Galerkin finite element method, using elliptic mesh generation equations coupled with time-dependent conservation equations, is applied to study slot coating flows of polymer solutions. The polymer molecules are represented by dumbbells with both linear and non-linear springs; hydrodynamic interactions between beads are incorporated. Calculations with infinitely extensible (Hookean) and pre-averaged finitely extensible (FENE-P) dumbbell models are performed and compared with equivalent closed-form macroscopic models in a conformation tensor based formulation [M. Pasquali, L.E. Scriven, Free surface flows of polymer solutions with models based on the conformation tensor, J. Non-Newtonian Fluid Mech. 108 (2002) 363–409]. The BCF equation for linear dumbbell models is solved using a fully implicit time integration scheme which is found to be more stable than the explicit Euler scheme used previously to compute complex flows. We find excellent agreement between the results of the BCF based formulation and the macroscopic conformation tensor based formulation. The computations using the BCF approach are stable at much higher Weissenberg numbers, $Wi = \lambda\dot{\gamma}$ (where λ is the characteristic relaxation time of polymer, and $\dot{\gamma}$ is the characteristic rate of strain) compared to the purely macroscopic conformation tensor based approach, which fail beyond a maximum Wi. A novel computational algorithm is introduced to compute complex flows with non-linear microscopic constitutive models (i.e. non-linear FENE dumbbells and dumbbells with hydrodynamic interactions) for which no closed-form constitutive equations exist. This algorithm is fast and computationally efficient when compared to both an explicit scheme and a fully implicit scheme involving the solution of the non-linear equations with Newton's method for each configuration field.

Keywords: Free surface flow; Finite element; Viscoelastic flow; Brownian configuration fields; Finite extensibility; Hydrodynamic interactions

1. Introduction

Free surface flows occur when a layer of liquid meets a gas at an interface. Such flows arise in a variety of commercial applications, such as coating (e.g. slot coating, roll coating, etc.), ink-jet printing, fiber spinning, and micropipetting. Frequently these applications involve liquids that are viscoelastic due to the presence of polymer as final product (e.g. coating) or as rheology modifier (e.g. ink-jet printing). Most of these flows are time dependent and their dynamics is controlled by the elasticity and capillarity of the liquid. Modeling such flows requires computational methods which can describe and predict the molecular conformation of polymers in the flow field while simultaneously capturing accurately the shape of free surfaces. The location of the free surface is unknown *a priori* in these problems and describing its evolution is a part of the solution to the problem. Different ways of handling free surface flows are discussed in detail in Refs. [1–5]. Due to the existence of a variety of industrial applications, Newtonian free surface flows have been studied extensively [6–11] . However, studies related to viscoelastic free surface flows are limited [12–17].

Here we study the flow in the downstream section of a slot coater. Slot coating belongs to a class of coating flows known as pre-metered coating, where the thickness of the coated layer is predetermined. Calculations of steady Newtonian [6–11] and viscoelastic slot coating flows [12,13,16] have been reported in literature; transient calculations have been attempted only recently [18]. Viscoelastic flows are usually modeled by adding an extra closed-form constitutive equation for the elastic stress. These constitutive equations are usually of rate-type, e.g. Oldroyd-B [19], FENE-P [19], etc. Such constitutive equations are obtained typically by approximating kinetic theory-based

* Corresponding author. Tel.: +1 713 348 5830; fax: +1 713 348 5478.
E-mail address: mp@rice.edu (M. Pasquali).

0377-0257/$ – see front matter © 2006 Elsevier B.V. All rights reserved.
doi:10.1016/j.jnnfm.2006.04.009

constitutive equations with the help of *closure approximations*. For instance, the FENE-P model is obtained by pre-averaging the fluctuating non-linear FENE force.

The conformation tensor based approach [12,20–22] introduces a microstructural variable representing the local state of the polymer solution (e.g. the conformation of polymer molecules in the solution). Pasquali and Scriven [12] used the conformation tensor based approach to study viscoelastic slot coating flows of ultra-dilute polymer solutions with different polymer models. They found that when the recirculation under the die lip was absent, all models failed at low *Wi* because of the singularity in the velocity gradient at the contact line (see also [23]). However, when a recirculation was present, much higher *Wi* could be achieved. The mode of failure was found to be independent of the model details, i.e., the smallest eigenvalue of the conformation tensor reached zero in the region of strong extensional flow under the stretching free surface. An important observation was that, in the presence of a recirculation, the maximum *Wi* achieved in all calculations increased as the model used to represent the polymer molecules captured the underlying physics more accurately. This suggests that shortcomings of these models could be due to the use of approximate non-linear kinetic theory based relations leading to a poor physical description of polymer molecules in solution.

Lee et al. [13] observed that viscoelasticity increases the meniscus invasion in slot coating flows and thus reduces the angle of separation at the static contact point. This has been identified as a possible mechanism for the onset of ribbing instabilities. A recent study by Romero et al. [16] has verified experimentally and theoretically that the viscoelastic nature of the fluid significantly reduces the contact angle, leading to a non-uniform coating.

With advances in the availability of computing power, a new method for simulating viscoelastic flows has emerged which avoids the need for a closed-form constitutive equation [24,25]. This approach, known as the micro–macro approach, combines the solution of macroscopic conservation equations with sophisticated non-linear kinetic theory based models for elastic stress evaluation. In essence, polymer molecules are represented by a micro-mechanical model which provides information on microstructural features such as the stretch and orientation of the molecules. Such models can incorporate important physics such as the finite extensibility of the polymer molecules and the presence of solvent mediated interactions such as hydrodynamic (HI) and excluded volume (EV) interactions between parts of the polymer chain [24,26]. The incorporation of these effects is necessary to explain experimentally observed features such as shear thinning and bounded extensional viscosity in homogeneous flows of dilute polymer solutions [19,26].

The CONNFFESSIT algorithm [25] was the first micro–macro-based method to be used and validated in one and two dimensional viscoelastic flow calculations [25,27–29]. It has also been successfully implemented to solve free surface flows [30,31]. The major problem of CONNFFESSIT is that a large number of particles must be convected with flow to reduce the statistical error bar on various flow variables. These particles must be tracked as they move in the flow field. A more efficient variant of this method, the Lagrangian particle method (LPM), has been applied successfully to solve viscoelastic flows [32]. While the LPM avoids the need of large number of discrete particles to reduce the error bar using correlated local ensembles, particle tracking still remains a problem. The problems of both particle tracking and spatial fluctuations are circumvented in the Brownian configuration fields method which also provides an efficient variance reduction in terms of temporal fluctuations. In the BCF method, proposed by Hulsen et al. [33], an ensemble of spatially correlated configuration fields replaces the discrete particles. The evolution of the ensemble is governed by a partial differential equation that can be solved on the same finite element mesh as the flow field. The main advantage of the BCF method over CONNFFESSIT and LPM is that the ensemble size is the same everywhere in the flow domain even for locally very refined meshes. However, with CONNFFESSIT and LPM, it is difficult to work with locally refined meshes as smaller elements might end up without any dumbbell in them. So far, the BCF method has been applied only to confined flows [33–35].

This paper extends the BCF method to solve transient viscoelastic free surface flows using a finite element algorithm. The algorithm is validated against exact closed-form macroscopic conformation tensor based models. We further extend the capabilities of BCF to FENE dumbbells and models with hydrodynamic interactions for which no closed-form equation can be derived. We present a new predictor–corrector time integration algorithm based on an earlier algorithm by Öttinger [24] to tackle the presence of non-linearities that aries due to the incorporation of a non-linear spring force and hydrodynamic interactions.

The next section presents an overview of the basic macroscopic conservation equations with a brief description of macroscopic and microscopic constitutive equations. The finite element implementation and time integration schemes are described in Section 3. Section 4 analyzes the flow under the downstream section of a slot coater, and Section 5 summarizes the conclusions of this paper.

2. Governing equations

2.1. Transport equations

The transport equations for mass and momentum in an unsteady, isothermal and incompressible flow of a dilute polymer solution in the absence of external forces are

$$0 = \nabla \cdot \mathbf{v} \tag{1}$$

$$0 = \rho \left(\frac{\partial \mathbf{v}}{\partial t} + \mathbf{v} \cdot \nabla \mathbf{v} \right) - \nabla \cdot \mathbf{T} \tag{2}$$

where $\mathbf{v}$ is the liquid velocity and ρ is the liquid density. The total stress tensor is $\mathbf{T} = -p\mathbf{I} + \boldsymbol{\tau} + \boldsymbol{\sigma}$, where p is the pressure, $\mathbf{I}$ the identity tensor, $\boldsymbol{\tau}$ the viscous stress tensor and $\boldsymbol{\sigma}$ is the polymer contribution to the total stress tensor. The viscous stress is: $\boldsymbol{\tau} = 2\eta_s \mathbf{D}$, where $\mathbf{D} = \frac{1}{2}(\nabla \mathbf{v} + \nabla \mathbf{v}^T)$ is the rate of strain tensor and η_s is the Newtonian viscosity.

Please cite this article as: Mohit Bajaj et al., Multiscale simulation of viscoelastic free surface flows, J. Non-Newtonian Fluid Mech. (2006), doi:10.1016/j.jnnfm.2006.04.009.

Table 1
Constitutive functions for Oldroyd-B and FENE-P models

	ξ	χ	g_0	g_1	g_2	a
Oldroyd-B	1	1	-1	1	0	$\frac{G}{2}\mathrm{tr}\,\mathbf{M}$
FENE-P	1	1	-1	$\frac{b_\mathbf{M}-1}{b_\mathbf{M}-\mathrm{tr}\,\mathbf{M}/3}$	0	$\frac{3G(b_\mathbf{M}-1)}{2}\ln\left(\frac{b_\mathbf{M}-1}{b_\mathbf{M}-\mathrm{tr}\,\mathbf{M}/3}\right)$

The polymer contribution $\boldsymbol{\sigma}$ to the total stress tensor can be evaluated either by using a macroscopic closed-form constitutive equation (e.g. Oldroyd-B or FENE-P) or from polymer kinetic theory [19,26] using the BCF method as discussed briefly below.

2.2. Macroscopic constitutive equation

The conformation tensor $\mathbf{M}$ is a microstructural variable that represents the local expectation value of the stretch and orientation of polymer molecules. In dilute solutions, the conformation tensor can be interpreted as the second moment of the end-to-end vector of an ensemble of polymer molecules:

$$\mathbf{M} = \int_{\mathbf{Q}\epsilon R^3} \mathbf{QQ}P(\mathbf{Q},t)\,\mathrm{d}\mathbf{Q} \tag{3}$$

where $\mathbf{Q}$ is the end-to-end vector, and $P(\mathbf{Q},t)\mathrm{d}\mathbf{Q}$ is the configurational distribution function which describes the number of polymer molecules whose end-to-end vectors lie between $\mathbf{Q}$ and $\mathbf{Q}+\mathrm{d}\mathbf{Q}$ at any given instant. Conformation tensor-based models have been shown to be thermodynamically consistent [20–22,36,37]. The invariants of the conformation tensor provide useful information on the microstructural state of the polymer. The eigenvectors of the conformation tensor represent the principal directions along which polymer chains are stretched, contracted, or oriented and its eigenvalues represents the square of principal stretch. The time evolution of the dimensionless conformation tensor is [37]:

$$\begin{aligned}0 = {} & \frac{\partial \mathbf{M}}{\partial t} + \mathbf{v}\cdot\nabla\mathbf{M} - 2\xi\frac{\mathbf{D}:\mathbf{M}}{\mathbf{I}:\mathbf{M}}\mathbf{M} \\ & - \chi\left(\mathbf{M}\cdot\mathbf{D}+\mathbf{D}\cdot\mathbf{M}-2\frac{\mathbf{D}:\mathbf{M}}{\mathbf{I}:\mathbf{M}}\mathbf{M}\right) - \mathbf{M}\cdot\boldsymbol{\varpi} - \boldsymbol{\varpi}^{\mathrm{T}}\cdot\mathbf{M} \\ & + \frac{1}{\lambda}(g_0\mathbf{I}+g_1\mathbf{M}+g_2\mathbf{M}^2)\end{aligned} \tag{4}$$

where $\boldsymbol{\varpi} = \frac{1}{2}(\nabla\mathbf{v} - \nabla\mathbf{v}^{\mathrm{T}})$ is the vorticity tensor, and λ is the characteristic relaxation time of the polymer. The constitutive function $\xi(\mathbf{M})$ represents the polymer's resistance to stretching along its backbone, $\chi(\mathbf{M})$ represents the polymer's resistance to orientation with respect to its neighbors and $g_0(\mathbf{M})$, $g_1(\mathbf{M})$, and $g_2(\mathbf{M})$ define the rate of relaxation of polymer segments. $R_\mathrm{e}^2/3$ is the length scale used to normalize the conformation tensor where R_e is the end-to-end distance of the polymer segment.

The elastic stress, $\boldsymbol{\sigma}$, is related to the conformation tensor by Pasquali and Scriven [37]:

$$\boldsymbol{\sigma} = 2(\xi-\chi)\frac{\mathbf{M}}{\mathbf{I}:\mathbf{M}}\mathbf{M} : \frac{\partial a}{\partial \mathbf{M}} + 2\chi\mathbf{M}\cdot\frac{\partial a}{\partial \mathbf{M}} \tag{5}$$

where $a(\mathbf{M})$, is the Helmholtz free energy per unit volume of the liquid.

Table 1 contains the constitutive functions ($\xi(\mathbf{M})$, $\chi(\mathbf{M})$, $g_0(\mathbf{M})$, $g_1(\mathbf{M})$, $g_2(\mathbf{M})$, and $a(T,\mathbf{M})$) for the Oldroyd-B and FENE-P models. The constitutive parameters are the polymer elastic moduls G, the relaxation time λ, and $b_\mathbf{M}$, the ratio of maximum length square of the polymer to its average length square at equilibrium in the FENE-P model.

2.3. Microscopic constitutive equation

Microscopic theories represent a polymeric liquid as an ensemble of non-interacting coarse-grained Brownian micromechanical models such as the bead-spring chain model [19,26]. The dumbbell model is the simplest in its class, and is used hereafter. A dumbbell consists of two Brownian beads with a friction coefficient ζ. The configurational state of a dumbbell is specified by the dumbbell connector vector $\mathbf{Q}$. The configurational distribution function, $P(\mathbf{Q},t)$ obeys the following Fokker–Planck or diffusion equation [26]:

$$\frac{\partial P}{\partial t} = -\frac{\partial}{\partial \mathbf{Q}}\cdot\left\{\nabla\mathbf{v}^{\mathrm{T}}\cdot\mathbf{Q} - \frac{2}{\zeta}\mathbf{A}\cdot\frac{\partial U}{\partial \mathbf{Q}}\right\}P + \frac{2k_\mathrm{B}T}{\zeta}\frac{\partial}{\partial \mathbf{Q}}\cdot\mathbf{A}\cdot\frac{\partial P}{\partial \mathbf{Q}} \tag{6}$$

where T is the temperature and k_B the Boltzmann's constant. The bead friction coefficient ζ is related to the Stokes drag as $\zeta = 6\pi\eta_\mathrm{s}a$ for spherical beads with radius a. The intermolecular potential energy U is the sum of the spring potential accounting for the polymer chain connectivity, and other local interactions such as excluded volume. In this work we have neglected excluded volume interactions and have only considered different spring potentials, which are related to the spring force $\mathbf{F}^\mathrm{s}$ by $\mathbf{F}^\mathrm{s} = \partial U/\partial\mathbf{Q}$. The tensor $\mathbf{A}$ is the diffusion tensor, whose form is discussed shortly below.

The spring force law $\mathbf{F}^\mathrm{s} = \Lambda\mathbf{Q}$. Here, $\Lambda = H$ for Hookean dumbbells, $\Lambda = H/(1-\langle Q^2\rangle/Q_0^2)$ for FENE-P dumbbells and $\Lambda = H/(1-Q^2/Q_0^2)$ for FENE dumbbells. H is the spring constant, Q_0 is the maximum extensibility of the spring and $\langle Q^2\rangle$ is the end-to-end distance of the dumbbell averaged over all the configurations of the dumbbell. The angular brackets denote an ensemble-average with respect to the configurational distribution function, i.e.:

$$\langle\mathbf{g}\rangle = \int P\mathbf{g}\,\mathrm{d}^3\mathbf{Q} \tag{7}$$

where $\mathbf{g}$ is any physical quantity.

In this case, $\sqrt{R_\mathrm{e}^2/3}$ is used as the length scale for the dumbbell connector $\mathbf{Q}$ where $R_\mathrm{e}^2 = \langle Q^2\rangle_\mathrm{eqm}/3$ with $\langle Q^2\rangle_\mathrm{eqm}$ representing the ensemble average of the end-to-end distance of a polymer molecule at equilibrium. The choice of $\sqrt{R_\mathrm{e}^2/3}$ as the length scale for the dumbbell connector is consistent with the

Please cite this article as: Mohit Bajaj et al., Multiscale simulation of viscoelastic free surface flows, J. Non-Newtonian Fluid Mech. (2006), doi:10.1016/j.jnnfm.2006.04.009.

length scale used to normalize the conformation tensor. The FENE parameter $b = 3Q_0^2/R_e^2$. In all our simulations we set $R_e^2/3 = 1$ and hence $b = Q_0^2$. Note that $b_{\mathbf{M}} = b/3$.

The diffusion tensor $\mathbf{A}$ is

$$\mathbf{A} = (\mathbf{I} - \zeta\boldsymbol{\Omega}) \tag{8}$$

where $\boldsymbol{\Omega}$ is the hydrodynamic interaction tensor which is represented by the regularized Oseen–Burgers tensor [38]:

$$\boldsymbol{\Omega}(\mathbf{Q}) = \frac{3\sqrt{3}\omega}{8\zeta Q\,(Q^2+\omega^2)^3}\left(M\mathbf{I} + N\frac{\mathbf{QQ}}{Q^2}\right) \tag{9}$$

Here, $\omega = 2h^*\sqrt{\pi k_B T/3H}$, $M = Q^6 + \frac{7}{2}\omega^2 Q^4 + \frac{9}{2}\omega^4 Q^2$ and $N = Q^6 + \frac{3}{2}\omega^2 Q^4 - \frac{3}{2}\omega^4 Q^2$. h^* is the hydrodynamic interaction parameter, $h^* = \zeta/\eta_s\{\sqrt{H/(36\pi^3 k_B T)}\}$.

The polymer contribution to the stress is given by

$$\boldsymbol{\sigma} = -nk_B T\mathbf{I} + n\langle\mathbf{Q}\,\mathbf{F}^s\rangle \tag{10}$$

where n is the number density of the dumbbells.

An alternative approach to obtaining the configuration average in Eq. (10) through solving the Fokker–Plank equation (6), is to obtain directly averages from trajectories of the connector vector $\mathbf{Q}$, determined from the stochastic differential equation (SDE) [24]:

$$\mathrm{d}\mathbf{Q} = \left[\nabla\mathbf{v}^{\mathrm{T}}\cdot\mathbf{Q} - \frac{2}{\zeta}\mathbf{A}\cdot\mathbf{F}^s\right]\mathrm{d}t + \sqrt{\frac{4k_B T}{\zeta}}(\mathbf{B}\cdot\mathrm{d}\mathbf{W}) \tag{11}$$

where $\mathrm{d}\mathbf{W}$ is a time-uncorrelated, Brownian force which accounts for the random displacement of the beads due to thermal motion, with zero mean and unit variance. The components of the tensor $\mathbf{B}(\mathbf{Q})$, which correspond to the diffusion term in Eq. (6), are chosen such that:

$$\mathbf{B}\cdot\mathbf{B}^{\mathrm{T}} = \mathbf{A} \tag{12}$$

It can be seen from Eqs. (8) and (9) that the tensor $\mathbf{A}$ has the form $g(\mathbf{Q})\mathbf{I} + \tilde{g}(\mathbf{Q})\mathbf{QQ}/Q^2$. Therefore, the tensor $\mathbf{B}$ can be chosen to be [24]:

$$\mathbf{B}(\mathbf{Q}) = \sqrt{g(\mathbf{Q})}\mathbf{I} + \left(\sqrt{g(\mathbf{Q})+\tilde{g}(\mathbf{Q})} - \sqrt{g(\mathbf{Q})}\right)\frac{\mathbf{QQ}}{Q^2} \tag{13}$$

Because the tensor $\mathbf{A}$ is a function of the configurations of dumbbells $\mathbf{Q}$, Eq. (12) must be solved for each dumbbell at every time step. Consequently, the number of equations represented by Eq. (13) depends on the ensemble size.

In the BCF approach, the (Lagrangian) stochastic ordinary differential equation (11) is converted into the (Eulerian) stochastic partial differential equation [33]:

$$\mathrm{d}\mathbf{Q} = \left[-\mathbf{v}\cdot\nabla\mathbf{Q} + \nabla\mathbf{v}^{\mathrm{T}}\cdot\mathbf{Q} - \frac{2}{\zeta}\mathbf{A}\cdot\mathbf{F}^s\right]\mathrm{d}t + \sqrt{\frac{4k_B T}{\zeta}}(\mathbf{B}\cdot\mathrm{d}\mathbf{W}) \tag{14}$$

The first term on the right-hand side of Eq. (14) accounts for the convection of the configuration field by the flow and $\mathbf{W}$ is a time-uncorrelated but *spatially homogeneous* Brownian force. The expression for stress calculation remains as Eq. (10).

2.4. Mesh generation

A boundary fitted elliptic mesh generation method proposed by de Santos [39] is used to construct the mapping between the physical domain and a reference or computational domain. The mapping obeys:

$$\nabla\cdot\tilde{\mathbf{D}}\cdot\nabla\boldsymbol{\xi} = 0 \tag{15}$$

where $\boldsymbol{\xi}$ is the position in the computational domain and the dyadic $\tilde{\mathbf{D}}$ controls the spacing of the coordinate lines [12].

The time dependent free surface flow problem is solved by the ALE algorithm [40–43]. The time derivatives of any scalar, vector or a tensor quantity Φ are transformed to time derivatives at fixed iso-parametric coordinates (denoted by $\overset{\circ}{\Phi}$) as

$$\frac{\partial\Phi}{\partial t} = \overset{\circ}{\Phi} - \overset{\circ}{\mathbf{x}}\cdot\nabla\Phi \tag{16}$$

where $\overset{\circ}{\mathbf{x}}$ is the mesh velocity.

2.5. Problem description and boundary conditions

Fig. 1 shows the downstream section of a slot coater. The upper wall is the die wall and the lower solid wall is the moving web. The liquid is being coated on the moving web. In pre-metered slot coating, the flow rate at the inlet and the final coating thickness are known. For the two dimensional flow in the downstream section of a slot coater considered in this work, Eqs. (1), (2), (4), (15), and (21) constitute a set of 13 scalar equations in 13 unknowns when solving for the flow field using the macroscopic approach, while Eqs. (1), (2), (14), and (15) are a set of $5 + 3N_f$ scalar equations when solving using the micro–macro approach, where N_f is the size of the ensemble. These equations are solved with boundary conditions on the transport and mesh equations as discussed below.

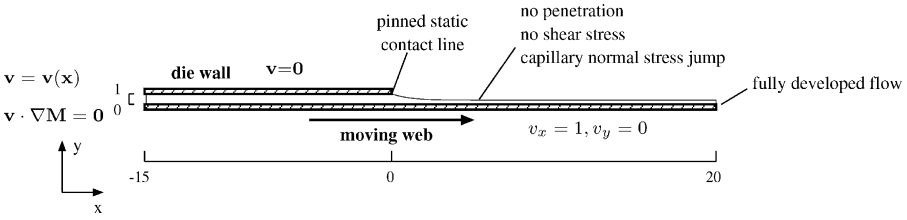

Fig. 1. Flow domain and boundary conditions used in analyzing the flow of viscoelastic liquid in the downstream section of a slot coater.

Please cite this article as: Mohit Bajaj et al., Multiscale simulation of viscoelastic free surface flows, J. Non-Newtonian Fluid Mech. (2006), doi:10.1016/j.jnnfm.2006.04.009.

2.5.1. Boundary conditions on transport equations

(1) A no slip boundary condition is applied at the solid walls (i.e. $\mathbf{v} = 0$ at the die wall while v_x = web velocity and $v_y = 0$ at the web).
(2) A force balance at the free surface is imposed as the boundary condition on the momentum equation through the following traction boundary condition:

$$\mathbf{n} \cdot \mathbf{T} = -p_a \mathbf{n} + \varsigma \mathbf{n}(\nabla_{II} \cdot \mathbf{n}) \tag{17}$$

where $\nabla_{II} = (\mathbf{I} - \mathbf{nn}) \cdot \nabla$ denotes the surface divergence operator [44], p_a is the ambient pressure in the gas phase and ς is the surface tension. $\mathbf{n}$ is the unit vector normal to the free surface.

This boundary condition is applied naturally through the boundary integration of the traction term ($\mathbf{n} \cdot \mathbf{T}$) in the momentum equation. As the normal vector $\mathbf{n}$ is discontinuous on the free surface, Eq. (17) cannot be used in its present form. Eq. (17) is integrated by parts before it is inserted into the traction term of the momentum equation. More details on the implementation of the traction boundary condition can be found, e.g., in Kistler and Schweizer [5], Ruschak [45] and Pasquali and Scriven [12].

(3) The flow rate at the inflow boundary is imposed by specifying a velocity profile $\mathbf{v} = f(\mathbf{x})$.
(4) The fully developed flow condition at the outflow boundary is imposed naturally as $\mathbf{n} \cdot \nabla \mathbf{v} = 0$.
(5) The conformation transport equation [Eq. (4)] is hyperbolic and the boundary condition on this equation is imposed in weighted residual form only at the inflow boundary. In fully developed flow, the polymer conformation does not change along the streamline [12,46] and thus:

$$\mathbf{v} \cdot \nabla \mathbf{M} = 0 \tag{18}$$

holds at the inflow boundary.
(6) The boundary condition on the configuration fields equation should be imposed at the inflow boundary where the configurations of the fields must be known. However, the configurations of the fields are not known in general, and for a given inflow velocity profile, the inflow configuration profile depends upon the type of spring force and the presence or absence of hydrodynamic interactions. In the literature, most viscoelastic flow calculations using the BCF method [33,34] are carried out either by imposing periodic boundary conditions or by calculating the configuration fields for a given velocity field (typically a linear or parabolic flow profile). Here, we propose a new way of imposing the inflow boundary condition on the BCF equation by assuming that the entry length is long enough to have a fully developed flow at the inlet boundary of the slot coater. Due to the fully developed flow between two parallel plates (Couette–Poiseuille flow in the slot coating die), the velocity and the velocity gradient do not change along streamlines. As a result, the evolution of configuration fields $\mathbf{Q}$ along the streamlines is independent of the flow field. The spatially correlated fields ensure that the gradient of $\mathbf{Q}$ remains zero, i.e.:

$$\mathbf{v} \cdot \nabla \mathbf{Q} = 0 \tag{19}$$

must hold at the inflow boundary. Eq. (19) is independent of the microscopic constitutive model and initial condition on configuration fields; it is applied weakly as a vector boundary condition by replacing the configuration fields residual at the inflow boundary.

2.5.2. Boundary conditions on mesh equations

The following boundary conditions are used to solve the mesh equation [Eq. (15)]:

(1) The location of nodes on the boundary is fixed at the inflow and on the two solid walls.
(2) At the free surface, the kinematic boundary condition:

$$\mathbf{n} \cdot (\overset{\circ}{\mathbf{x}} - \mathbf{v}) = 0 \tag{20}$$

is applied in the weak form.

2.6. Initial conditions

Initial conditions are required to solve the momentum, conformation tensor and the configuration field equations. For transient computations, initial conditions for various field variables are described in Section 4.3. For steady flow computations, the initial conditions used for the Brownian dynamics simulation (BDS) to solve the configuration fields equation are as follows.

For BDS of Hookean dumbbells, all configuration fields are assumed to be spatially uniform initially and their values are independently sampled from the equilibrium distribution function of the Hookean dumbbell model. However, for FENE and FENE-P dumbbells, BD simulations were started with an equilibrium ensemble of Hookean dumbbells which were subsequently allowed to relax for three to five relaxation times in order to obtain the correct equilibrium distribution in these cases. The simulations for $Wi > 2$ are performed by using the configurations of Brownian fields at lower Wi as initial condition.

3. Computational method

3.1. Macroscopic approach

The conservation equations are discretized by the DEVSS-TG (discrete elastic viscous stress split-traceless gradient) mixed finite element method [12]. DEVSS-TG method is a stable formulation which has been developed as an improvement over the earlier DEVSS schemes by Guénette et al. [47] and Guénette and Fortin [48] where an additional field variable for the traceless interpolated velocity gradient $\mathbf{L}$ is introduced and computed with other variables (see [12] for more details). The tensorial equation for $\mathbf{L}$ is

$$0 = \mathbf{L} - \nabla \mathbf{v} + \frac{1}{\mathrm{tr}\,\mathbf{I}}(\nabla \cdot \mathbf{v})\mathbf{I} \tag{21}$$

For two dimensional slot coating flow computations carried out in this work $\mathrm{tr}\,\mathbf{I} = 2$.

Please cite this article as: Mohit Bajaj et al., Multiscale simulation of viscoelastic free surface flows, J. Non-Newtonian Fluid Mech. (2006), doi:10.1016/j.jnnfm.2006.04.009.

Eqs. (1), (2), (15) and (21) are written in the weighted residual form using Galerkin weighting functions. Eq. (4) is weighted with the Streamline Upwind Petrov Galerkin (SUPG [49]) weighting functions. All independent variables are then represented by finite element basis functions as: $\mathbf{\Phi} = \sum_\beta \Phi^\beta \varphi^\beta$, where $\mathbf{\Phi}$ is a vector, dyadic or scalar [$\mathbf{v}$, p, $\mathbf{x}$, $\mathbf{L}$, $\mathbf{M}$], φ^β are the basis functions [$\varphi^\beta_{\mathbf{v}}$, $\varphi^\beta_{\mathrm{p}}$, $\varphi^\beta_{\mathbf{x}}$, $\varphi^\beta_{\mathbf{L}}$, $\varphi^\beta_{\mathbf{M}}$] and Φ^β are the unknown coefficients [$\mathbf{v}^\beta$, p^β, $\mathbf{x}^\beta$, $\mathbf{L}^\beta$, $\mathbf{M}^\beta$]. Continuous biquadratic basis functions represent velocity and position, linear discontinuous basis functions represent pressure and continuous bilinear basis functions are used for the interpolated velocity gradient and conformation tensor.

The DEVSS-TG/SUPG spatial discretization results in a large set of differential–algebraic equations, $\mathbf{f}(t, \mathbf{y}, \dot{\mathbf{y}}) = 0$, for the vector of time dependent unknowns $\mathbf{y} = [\mathbf{v}, p, \mathbf{x}, \mathbf{L}, \mathbf{M}]$. A fully implicit predictor–corrector scheme [50] is used for time integration. A first order forward Euler predictor with first order backward Euler corrector steps is used for the first few time steps to ensure time smoothing [51]. Subsequently, a second order Adams–Bashforth predictor with second order trapezoidal rule corrector is used (see [50,52] for more details). The resulting set of coupled nonlinear equations are then solved using a frontal solver algorithm with Newton's method and analytical Jacobian at each time step [12].

3.2. Micro–macro approach

In the BCF based micro–macro approach, the Galerkin finite element method is used to discretize spatially the mapping, continuity and momentum equations together with the SUPG [49] formulation of the BCF equation [35]. The interpolated velocity gradient is not necessary in this formulation. Bilinear continuous basis functions are used to approximate the configuration fields. The evolution of the system is computed at each time step by first fixing the polymer contribution to the stress and computing the position, velocity, and pressure with a fully implicit time integration scheme and Newton's method. The BCF equation is then solved to update the polymer contribution to stress using fixed flow kinematics.

Two different time integration schemes, namely, a fully implicit time integration scheme for linear dumbbell models without hydrodynamic interactions and a semi-implicit time integration scheme for non-linear dumbbell models (FENE) or linear dumbbells with hydrodynamic interactions, are used to integrate the BCF equation. The two schemes are discussed below.

3.2.1. Fully implicit scheme

For the linear spring force without hydrodynamic interactions (i.e. with the diffusion tensor replaced with a unit tensor, $\mathbf{A} = \mathbf{B} = \mathbf{I}$) Eq. (14) can be rewritten as

$$\mathrm{d}\mathbf{Q} = \left(-\mathbf{v}\cdot\nabla\mathbf{Q} + \nabla\mathbf{v}^{\mathrm{T}}\cdot\mathbf{Q} - \frac{2\Lambda}{\zeta}\mathbf{Q}\right)\mathrm{d}t + \sqrt{\frac{4k_{\mathrm{B}}T}{\zeta}}\,\mathrm{d}\mathbf{W}(t) \tag{22}$$

Eq. (22) is discretized temporally using an implicit Euler scheme as

$$\mathbf{Q}_{n+1} = \mathbf{Q}_n + \left(-\mathbf{v}_n\cdot\nabla\mathbf{Q}_{n+1} + \nabla\mathbf{v}_n^{\mathrm{T}}\cdot\mathbf{Q}_{n+1} - \frac{2\Lambda_n}{\zeta}\mathbf{Q}_{n+1}\right) \times \Delta t + \sqrt{\frac{4k_{\mathrm{B}}T}{\zeta}}\,\Delta\mathbf{W}_n \tag{23}$$

where n is the previous and $(n+1)$ is the current time step. Λ_n is a function of field's configurations for FENE-P dumbbells evaluate at the previous time step. Eq. (23) can be rearranged as

$$\mathbf{Q}_{n+1} + \left(\mathbf{v}_n\cdot\nabla\mathbf{Q}_{n+1} - \nabla\mathbf{v}_n^{\mathrm{T}}\cdot\mathbf{Q}_{n+1} + \frac{2\Lambda_n}{\zeta}\mathbf{Q}_{n+1}\right) \times \Delta t = \mathbf{Q}_n + \sqrt{\frac{4k_{\mathrm{B}}T}{\zeta}}\,\Delta\mathbf{W}_n \tag{24}$$

The weak form of this equation is

$$\int_\Omega \left[\mathbf{Q}_{n+1} + \left(\mathbf{v}_n\cdot\nabla\mathbf{Q}_{n+1} - \nabla\mathbf{v}_n^{\mathrm{T}}\cdot\mathbf{Q}_{n+1} + \frac{2\Lambda_n}{\zeta}\mathbf{Q}_{n+1}\right)\Delta t\right] \times \psi^\alpha_{\mathbf{Q}}\,\mathrm{d}\Omega - \int_\Omega \left[\mathbf{Q}_n + \sqrt{\frac{4k_{\mathrm{B}}T}{\zeta}}\,\Delta\mathbf{W}_n\right]\psi^\alpha_{\mathbf{Q}}\,\mathrm{d}\Omega = 0 \tag{25}$$

where $\psi^\alpha_{\mathbf{Q}}$ is the weighing function for configuration fields equation and Ω is the physical domain. The configuration field $\mathbf{Q}$ is expanded as $\mathbf{Q} = \sum_\beta \mathbf{Q}^\beta \varphi^\beta_{\mathbf{Q}}$ where $\mathbf{Q}^\beta$ represent coefficients and $\varphi^\beta_{\mathbf{Q}}$ are basis functions. Thus:

$$\sum_\beta \mathbf{K}^{\alpha\beta}\mathbf{\Upsilon}^\beta_{n+1} = \mathbf{f}^\alpha \tag{26}$$

where the components of the matrix $\mathbf{K}^{\alpha\beta}$ for Hookean dumbbell are

$$\mathbf{K}^{\alpha\beta}_{ij} = \int_\Omega \left[\varphi^\beta_{\mathbf{Q}}\,\delta_{ij} + \left\{(\mathbf{v}_n\cdot\nabla\varphi^\beta_{\mathbf{Q}})\,\delta_{ij} - \varphi^\beta_{\mathbf{Q}}(\nabla_j v_i{}^{\mathrm{T}})_n + \frac{2\varphi^\beta_{\mathbf{Q}}H}{\zeta}\delta_{ij}\right\}\Delta t\right]\psi^\alpha_{\mathbf{Q}}\,\mathrm{d}\Omega \tag{27}$$

and for FENE-P dumbbell are

$$\mathbf{K}^{\alpha\beta}_{ij} = \int_\Omega \left[\varphi^\beta_{\mathbf{Q}}\,\delta_{ij} + \left\{(\mathbf{v}_n\cdot\nabla\varphi^\beta_{\mathbf{Q}})\,\delta_{ij} - \varphi^\beta_{\mathbf{Q}}(\nabla_j v_i{}^{\mathrm{T}})_n + \frac{2\,\varphi^\beta_{\mathbf{Q}}H}{\zeta(1-\langle Q_n^2\rangle/b)}\delta_{ij}\right\}\Delta t\right]\psi^\alpha_{\mathbf{Q}}\,\mathrm{d}\Omega \tag{28}$$

δ_{ij} representing the Kronecker delta. In Eq. (26) $\mathbf{\Upsilon}^\beta_{j,n+1}$ is a vector of the coefficients of configuration fields ($Q^\beta_{j,n+1}$) and

$$f^\alpha_i = \int_\Omega \left[Q_{i,n} + \sqrt{\frac{4k_{\mathrm{B}}T}{\zeta}}\,\Delta W_{i,n}\right]\psi^\alpha_{\mathbf{Q}}\,\mathrm{d}\Omega \tag{29}$$

Eq. (26) is assembled to obtain a global set of equations which in matrix vector form can be written as

$$\mathbf{K}\mathbf{\Upsilon}_{n+1} = \mathbf{f} \tag{30}$$

Please cite this article as: Mohit Bajaj et al., Multiscale simulation of viscoelastic free surface flows, J. Non-Newtonian Fluid Mech. (2006), doi:10.1016/j.jnnfm.2006.04.009.

The set of linear equations (30) can be solved using LU decomposition of the matrix **K** followed by back substitution. For Hookean dumbbells, the matrix **K** is independent of the configurations of the dumbbells. However, for FENE-P dumbbells, the matrix **K** is a function of the configuration of the dumbbells evaluated at the previous time step [see Eq. (28)]. It should be noted that the LU decomposition of the matrix **K** is performed at each time step because the mesh changes at each time step and **K** depends on the mesh. Eq. (30) is the global equation set for a single configuration field. However, as the configuration fields are independent of each other, Eq. (30) holds for all the fields except that the Brownian force term and $Q_{i,n}$ in Eq. (29) is different for each field.

3.2.2. Semi-implicit predictor corrector scheme

This scheme was originally developed by Öttinger [24] for FENE dumbbells in homogeneous flows and has been recently extended to finitely extensible bead-spring chains with and without hydrodynamic interactions in homogeneous flows [53–55]. The semi-implicit formulation leads to greater stability of the numerical algorithm [24,53,54] when compared to the explicit Euler scheme, and allows larger time steps. Somasi et al. [54] compared the semi-implicit scheme to an explicit Euler algorithm with rejections to compute flow of non-linear dumbbells. They showed that for a given accuracy the semi-implicit predictor–corrector is three to four times faster than the explicit Euler with rejection. Somasi and Khomami [35] have used the semi-implicit scheme for micro–macro simulations of FENE dumbbells in homogeneous flows. Here, we extend the same scheme to inhomogeneous flows of non-linear dumbbells with hydrodynamic interactions.

In the predictor step, the configuration fields are updated explicitly using forward Euler as

$$\mathbf{Q}^*_{n+1} = \mathbf{Q}_n + \left[-\mathbf{v}_n\cdot\nabla\mathbf{Q}_n + \nabla\mathbf{v}_n^{\mathrm{T}}\cdot\mathbf{Q}_n - \frac{2}{\zeta}\mathbf{A}_n\cdot\mathbf{F}^{\mathrm{s}}_n\right]\Delta t + \sqrt{\frac{4k_{\mathrm{B}}T}{\zeta}}(\mathbf{B}_n\cdot\Delta\mathbf{W}_n) \tag{31}$$

where $\mathbf{Q}^*_{n+1}$ are the predicted configuration fields. The finite element discretization yields the following matrix vector form:

$$\sum_\beta \mathbf{M}^{\alpha\beta}\boldsymbol{\Upsilon}^{\beta,*}_{n+1} = \mathbf{f}^\alpha \tag{32}$$

where $\mathbf{M}^{\alpha\beta}$ is the mass matrix of following form:

$$\mathbf{M}^{\alpha\beta} = \int_\Omega \psi^\alpha_{\mathbf{Q}}\varphi^\beta_{\mathbf{Q}}\mathbf{I}\,\mathrm{d}\Omega \tag{33}$$

$\boldsymbol{\Upsilon}^{\beta,*}_{n+1}$ is a vector of the coefficients of configuration fields basis functions ($\mathbf{Q}^{\beta,*}_{n+1}$) and $\mathbf{f}^\alpha$ is

$$\mathbf{f}^\alpha = \int_\Omega \left[\mathbf{Q}_n + \left(-\mathbf{v}_n\cdot\nabla\mathbf{Q}_n + \nabla\mathbf{v}_n^{\mathrm{T}}\cdot\mathbf{Q}_n - \frac{2}{\zeta}\mathbf{A}_n\cdot\mathbf{F}^{\mathrm{s}}_n\right)\Delta t + \sqrt{\frac{4k_{\mathrm{B}}T}{\zeta}}(\mathbf{B}_n\cdot\Delta\mathbf{W}_n)\right]\psi^\alpha_{\mathbf{Q}}\,\mathrm{d}\Omega \tag{34}$$

Eq. (32) is assembled into a global set of linear equations which is solved using LU decomposition of the mass matrix performed at each time step.

Estimates of configuration fields generated at the predictor step ($\mathbf{Q}^*_{n+1}$) are used in constructing the corrector:

$$\mathbf{Q}_{n+1} = \mathbf{Q}_n - \frac{\Delta t}{2}(\mathbf{v}_n\cdot\nabla\mathbf{Q}^*_{n+1} + \mathbf{v}_n\cdot\nabla\mathbf{Q}_n) + \frac{\Delta t}{2}(\nabla\mathbf{v}_n^{\mathrm{T}}\cdot\mathbf{Q}^*_{n+1} + \nabla\mathbf{v}_n^{\mathrm{T}}\cdot\mathbf{Q}_n) - \frac{\Delta t}{\zeta}\mathbf{A}_n\cdot(\mathbf{F}^{\mathrm{S}}_n + \mathbf{F}^{\mathrm{S}}_{n+1}) + \sqrt{\frac{4k_{\mathrm{B}}T}{\zeta}}(\mathbf{B}_n\cdot\Delta\mathbf{W}_n) \tag{35}$$

here, the $\mathbf{A}_n$ and $\mathbf{B}_n$ are the same as used in Eq. (31). The force term, however, is treated *implicitly*, with the term $\mathbf{F}^{\mathrm{S}}_{n+1}$ being evaluated using $\mathbf{Q}_{n+1}$. Following Ref. [53] and writing

$$\mathbf{A}_n\cdot\mathbf{F}^{\mathrm{S}}_{n+1} \approx \mathbf{F}^{\mathrm{S}}_{n+1} - \zeta(\boldsymbol{\Omega}_n\cdot\mathbf{F}^{\mathrm{S}}_n) \tag{36}$$

Eq. (35) can be simplified further

$$\mathbf{Q}_{n+1} + \frac{\Delta t}{\zeta}\mathbf{F}^{\mathrm{S}}_{n+1} = \mathbf{Q}_n - \frac{\Delta t}{2}(\mathbf{v}_n\cdot\nabla\mathbf{Q}^*_{n+1} + \mathbf{v}_n\cdot\nabla\mathbf{Q}_n) + \frac{\Delta t}{2}\left(\nabla\mathbf{v}_n^{\mathrm{T}}\cdot\mathbf{Q}^*_{n+1} + \nabla\mathbf{v}_n^{\mathrm{T}}\cdot\mathbf{Q}_n\right) - \frac{\Delta t}{\zeta}(\mathbf{A}_n\cdot\mathbf{F}^S_n) + \Delta t(\boldsymbol{\Omega}_n\cdot\mathbf{F}^S_n) + \sqrt{\frac{4k_{\mathrm{B}}T}{\zeta}}(\mathbf{B}_n\cdot\Delta\mathbf{W}_n) \tag{37}$$

For FENE dumbbells, $\mathbf{F}^{\mathrm{s}} = H\mathbf{Q}/(1-Q^2/b)$ can be substituted into Eq. (37), which can then be rearranged into the following form:

$$\left(1 - \frac{Q^2_{n+1}}{b} + \frac{H\,\Delta t}{\zeta}\right)\mathbf{Q}_{n+1} - \left(1 - \frac{Q^2_{n+1}}{b}\right)\boldsymbol{\Gamma} = 0 \tag{38}$$

where $\boldsymbol{\Gamma}$ is the right-hand side of Eq. (37). $\boldsymbol{\Gamma}$ is a function of the predicted values of the connector vector and of quantities whose values at the previous time step are known. We solve Eq. (38) in two distinct ways as follows.

3.2.2.1. Newton's method with a rejection algorithm. The finite element discretization of Eq. (38) results in a set of non-linear equations for each configuration field which can be solved with Newton's method. Thus, for each configuration field:

$$\sum_\beta \mathbf{J}^{\alpha\beta}\Delta\boldsymbol{\Upsilon}^\beta_{n+1} = -\mathbf{r}^\alpha \tag{39}$$

where $\Delta\boldsymbol{\Upsilon}^\beta_{n+1} = \boldsymbol{\Upsilon}^\beta_{n+1} - \boldsymbol{\Upsilon}^\beta_{0,n+1}$ with $\boldsymbol{\Upsilon}^\beta_{n+1}$ denoting a vector of the coefficients of configuration fields ($\mathbf{Q}^\beta_{n+1}$) at the current Newton iteration and $\boldsymbol{\Upsilon}^\beta_{0,n+1}$ is a vector of the coefficients of configuration fields ($\mathbf{Q}^\beta_{0,n+1}$) at the previous Newton iteration.

Please cite this article as: Mohit Bajaj et al., Multiscale simulation of viscoelastic free surface flows, J. Non-Newtonian Fluid Mech. (2006), doi:10.1016/j.jnnfm.2006.04.009.

$\mathbf{r}^{\alpha}$ is the residual vector given by

$$\mathbf{r}_i^{\alpha} = \int_{\Omega} \left[\left(1 - \frac{Q_{n+1}^2}{b} + \frac{H\,\Delta t}{\zeta} \right) Q_{i,\,n+1} - \left(1 - \frac{Q_{n+1}^2}{b} \right) \Gamma_i \right] \times \psi_{\mathbf{Q}}^{\alpha}\, \mathrm{d}\Omega \tag{40}$$

evaluated using the configuration fields at the previous Newton iteration.

$\mathbf{J}^{\alpha\beta}$ is the Jacobian matrix obtained by differentiating Eq. (38) with respect to $\mathbf{Q}_{n+1}^{\beta}$ (see Appendix A for a derivation of the Jacobian matrix). The components of $\mathbf{J}^{\alpha\beta}$ are

$$\mathbf{J}_{ij}^{\alpha\beta} = \int_{\Omega} \left[\left(1 - \frac{Q_{n+1}^2}{b} + \frac{H\,\Delta t}{\zeta} \right) \delta_{ij} - \frac{2}{b} Q_{i,n+1} Q_{j,n+1} + \frac{2}{b} \Gamma_i Q_{j,n+1} \right] \psi_{\mathbf{Q}}^{\alpha} \varphi_{\mathbf{Q}}^{\beta}\, \mathrm{d}\Omega \tag{41}$$

evaluated using the configuration fields at the previous Newton iteration.

Newton's method is expensive for calculations for FENE dumbbells because of the large number of configuration fields and because the Jacobian matrix depends on the field's configuration. However, an approximate analytical Jacobian can be derived by replacing Q_{n+1}^2 in Eq. (38) by $\langle Q_n^2 \rangle$ only in the derivation of the Jacobian matrix. The approximate Jacobian has the following form:

$$\mathbf{J}_{ij}^{\alpha\beta} = \int_{\Omega} \left(1 - \frac{\langle Q_n^2 \rangle}{b} + \frac{H\,\Delta t}{\zeta} \right) \psi_{\mathbf{Q}}^{\alpha} \varphi_{\mathbf{Q}}^{\beta} \delta_{ij}\, \mathrm{d}\Omega \tag{42}$$

$\langle Q_n^2 \rangle$ is evaluated at the previous time step; thus, Eq. (42) is independent of the configurations of the fields at the current time step and the LU factorization of the Jacobian matrix is done only once per time step for all the fields. Eq. (42) was used as an approximate Jacobian except for those fields for which the desired convergence (10^{-5}) was not achieved in a given number of Newton iterations. For such cases, the exact Jacobian was used. During the course of Newton iterations any field whose magnitude stretched beyond its maximum length ($\sqrt{b}$) for FENE dumbbells, was reset to $0.98\sqrt{b}$.

3.2.2.2. Least-squares collocation method (LSC). Eq. (38) can be rearranged into a cubic equation for the magnitude of $\mathbf{Q}_{n+1}$, which has been shown by Öttinger [24] to have unique solution between 0 and $\sqrt{b}$:

$$|Q_{n+1}|^3 - |\Gamma||Q_{n+1}|^2 - b\left(1 + \frac{H\,\Delta t}{\zeta} \right) |Q_{n+1}| + |\Gamma| b = 0 \tag{43}$$

where $|Q_{n+1}|$ is the magnitude of $\mathbf{Q}_{n+1}$ and $|\Gamma|$ is the magnitude of $\mathbf{\Gamma}$. In the LSC method, Eq. (43) is solved at collocation points, which here are chosen to coincide with the Gauss integration points. Eq. (43) can be solved at these collocation points in each element either analytically or numerically. The collocation solution is then projected onto the mesh using a least-square projection as discussed below.

Let $|Q_{n+1}| = y$ be the solution of the cubic equation; then, at each collocation (Gauss) point:

$$\tilde{\mathbf{Q}}_{n+1} = \left(\frac{\mathbf{\Gamma}}{|\Gamma|} \right) y \tag{44}$$

The least square projection is

$$\int_{\Omega} (\mathbf{Q}_{n+1} - \tilde{\mathbf{Q}}_{n+1}) \psi^{\alpha}\, \mathrm{d}\Omega = 0 \tag{45}$$

The finite element discretization of Eq. (45) results in a set of linear equations which in matrix vector form can be written as

$$\sum_{\beta} \mathbf{M}^{\alpha\beta} \mathbf{\Upsilon}_{n+1}^{\beta} = \mathbf{f}^{\alpha} \tag{46}$$

where $\mathbf{M}^{\alpha\beta}$ is the mass matrix given by Eq. (33), $\mathbf{\Upsilon}_{n+1}^{\beta}$ is the vector of coefficients of the configuration fields and

$$\mathbf{f}^{\alpha} = \int_{\Omega} \tilde{\mathbf{Q}}_{n+1} \psi_{\mathbf{Q}}^{\alpha}\, \mathrm{d}\Omega \tag{47}$$

which can be evaluated trivially by Gaussian quadrature because $\tilde{\mathbf{Q}}_{n+1}$ is known at all Gauss points. Eq. (46) is solved using LU decomposition of the mass matrix followed by back substitution. The mass matrix in Eq. (46) is the same as the mass matrix evaluated at the predictor step and hence there is no extra computational cost involved in computing and decomposing the mass matrix at the corrector step.

For linear dumbbells with hydrodynamic interactions (which is treated explicitly), Eq. (37) is linear in the connector vector $\mathbf{Q}_{n+1}$ and can be written as

$$\mathbf{Q}_{n+1} = \frac{\mathbf{\Gamma}}{1 + (\Lambda_n\, \Delta t/\zeta)} \tag{48}$$

where $\mathbf{\Gamma}$ is the right-hand side of Eq. (37) with a linear spring force. $\Lambda_n = H$ for Hookean dumbbells and for FENE-P dumbbells $\Lambda_n = H/(1 - \langle Q_n^2 \rangle / b)$. For linear dumbbell models both Newton's method and the LSC method are identical. As a result, the latter method can be used to evaluate the nodal values of $\mathbf{Q}_{n+1}$ from Eq. (48). The fully implicit scheme discussed earlier is not appropriate for linear dumbbells with hydrodynamic interactions because of the non-linear terms in the hydrodynamic interaction tensor $\mathbf{\Omega}$.

Eq. (48) can be formulated in the form of with Eq. (46) as, with

$$\mathbf{f}^{\alpha} = \int_{\Omega} \frac{\mathbf{\Gamma}}{1 + (\Lambda_n \Delta t/\zeta)} \psi_{\mathbf{Q}}^{\alpha}\, \mathrm{d}\Omega \tag{49}$$

The global mass matrix is the same as the mass matrix evaluated at the predictor step.

3.3. Dimensionless numbers

Dimensional analysis of the system of equations suggests that it is convenient to introduce four dimensionless numbers, which are combinations of the various macroscopic model parameters ρ, L, η_s, ς, v, $\eta_{p,0}$, λ, ρ, etc. These dimensionless numbers are:

Please cite this article as: Mohit Bajaj et al., Multiscale simulation of viscoelastic free surface flows, J. Non-Newtonian Fluid Mech. (2006), doi:10.1016/j.jnnfm.2006.04.009.

(1) The Reynolds number $Re = \rho v L/(\eta_s + \eta_{p,0})$ where v is the web speed and L is the height of the gap between the web and the die.
(2) The Capillary number $Ca = (\eta_s + \eta_{p,0})v/\varsigma$.
(3) The viscosity ratio $\beta = \eta_s/(\eta_s + \eta_{p,0})$.
(4) The Weissenberg number $Wi = \lambda_\eta v/L$, where λ_η is the characteristic relaxation time of polymer. The definition of λ_η used here (see Appendix B) is based on the zero shear rate viscosity.

In all the simulations reported here, we set $Re = 0$, by choosing $\rho = 0$. Similarly, we set $Ca = 0.1$. This is achieved by choosing $v = 1$, $\eta = \eta_s + \eta_{p,0} = 1$, and $\varsigma = 10$. In addition to keeping Re and Ca fixed, all simulations are performed at a dimensionless flow rate 0.3, for which a recirculation region is always present in the flow domain [12]. The only dimensionless numbers that are varied in this work are β and Wi. Basically, two different values of β have been studied ($\beta = 0.75$ and 1.0), while simulations have been carried out for a wide range of values of Wi. Since $\eta = 1$, and in addition we choose $L = 1$, variation in Wi and β is achieved by varying λ_η and η_s (and consequently $\eta_{p,0}$). Time is expressed in units of the polymer longest relaxation time.

In micro–macro simulations λ_η is related to microscopic parameters, such as H, ζ, h^*, etc., with a relationship that depends on the particular microscopic model. In order to compare results of different models at identical values of Wi, it becomes important, consequently, to choose appropriate values for these microscopic parameters. The scheme used here to determine these parameters is discussed in detail in Appendix B.

4. Results and discussion

The convergence of the numerical solutions is tested on four different meshes. Details of the meshes M1, M2, M3 and M4 are given in Table 2. Fig. 2 displays the portion of the meshes near the contact line. Elements are concentrated near the free surface to capture the steep layers of conformations at high Wi.

In the macroscopic method, steady state flows can be computed directly. This is not possible with the micro–macro approach. Except where explicitly indicated, all the macroscopic steady flows are computed directly hereafter.

4.1. Comparison of linear dumbbell models with equivalent conformation tensor based models

Because this work represents the first attempt to extend the BCF method to solve complex free surface flows, we validate our numerical scheme by comparing results for linear dumbbell models using the macroscopic and the micro–macro method for both ultra-dilute and dilute polymer solutions.

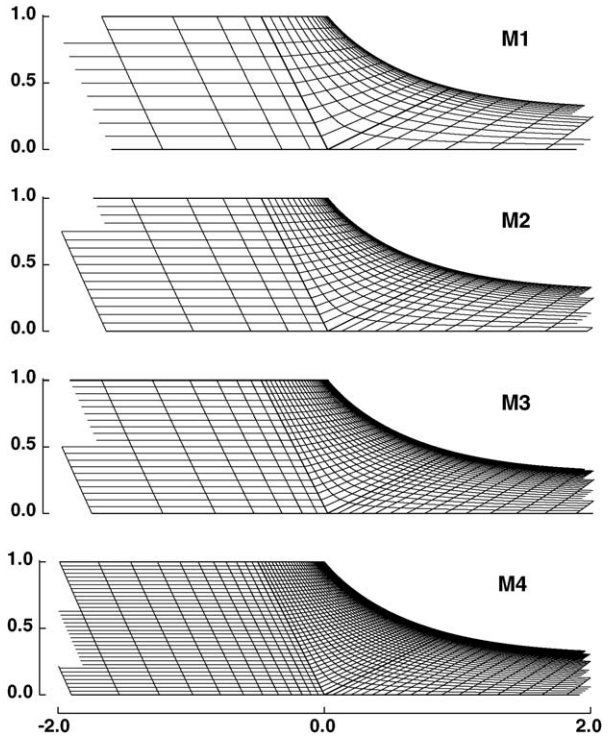

Fig. 2. Meshes used in analyzing the downstream section of slot coater.

4.1.1. Ultra-dilute solutions

The flow of an ultra-dilute polymer solution is computed by setting $\eta_p = 0$, i.e. $\beta = 1$. In this situation the evolution equations for the conformation tensor and for configuration fields are decoupled from the mass, momentum and mesh equations. Thus for a given Newtonian solution, the distribution of polymer conformation in flow is investigated by solving the conformation tensor and configuration fields equations. The slot coating flow of an ultra-dilute solutions using the conformation tensor model has been studied earlier (on different meshes) by Pasquali and Scriven [12].

Fig. 3 shows the largest and smallest eigenvalues of the conformation tensor in the flow domain as a function of Wi for the Oldroyd-B and FENE-P models using the macroscopic method. As shown in Fig. 3 computations using different meshes breakdown at different values of Wi, i.e. the smallest eigenvalue of the conformation tensor becomes negative in certain regions of the flow field [12]. The maximum Wi achieved in these computations

Table 2
Meshes used for slot coating flow computations

Mesh	Number of elements	Number of nodes	Degrees of freedom for fully coupled macroscopic simulations (**x**, **v**, p, **M**, **L**)	Degrees of freedom for micro–macro simulations
M1	550	2311	15712	10894 (**x**, **v**, p) and 1818 (**Q**)
M2	1096	4539	30836	21444 (**x**, **v**, p) and 3522 (**Q**)
M3	2100	8611	58392	
M4	4105	16717	113215	

Micro–macro computations are done only with M1 and M2 meshes.

Please cite this article as: Mohit Bajaj et al., Multiscale simulation of viscoelastic free surface flows, J. Non-Newtonian Fluid Mech. (2006), doi:10.1016/j.jnnfm.2006.04.009.

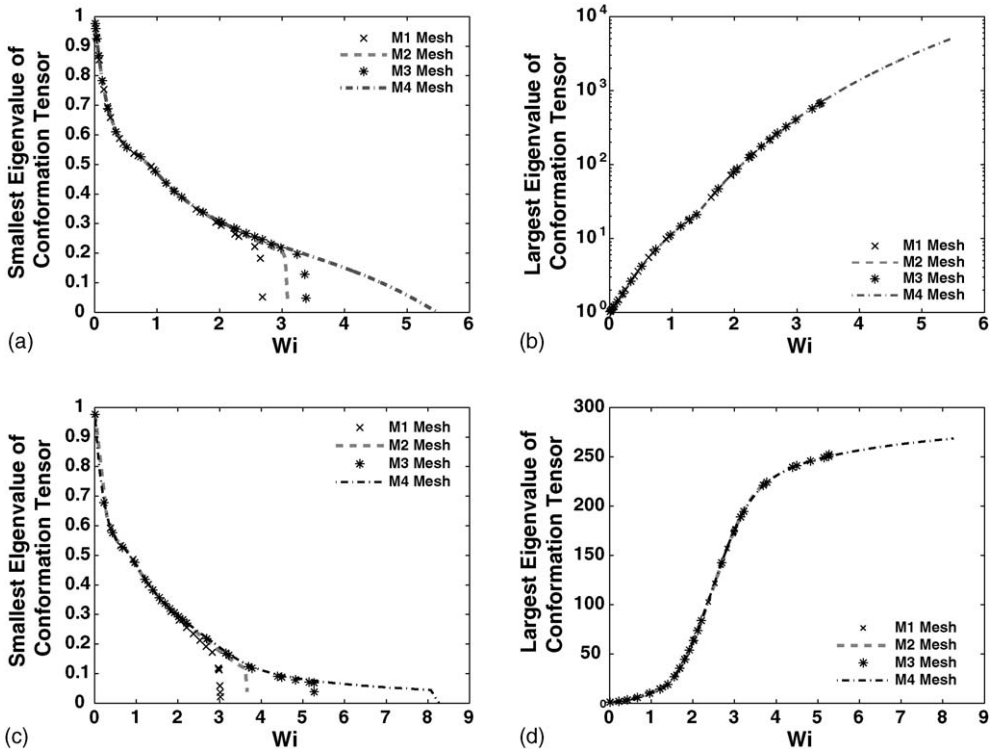

Fig. 3. Largest and smallest eigenvalues of the conformation tensor in the flow domain for an ultra-dilute solution of Oldroyd-B liquid using the macroscopic approach [(a) and (b)] and a FENE-P liquid [(c) and (d)]. $Ca = 0.1$, $Q = 0.3$, $\beta = 1.0$, $b_{\mathbf{M}} = 100$.

for ultra-dilute solutions grows with mesh refinement (Table 3). Stress boundary layers are formed under the free surface and these boundary layers cannot be captured beyond a certain *Wi* for a given mesh resolution. The evolution of the M_{xx} component of conformation tensor for the Oldroyd-B model with increasing *Wi* is displayed in Fig. 4. As *Wi* increases, both conformation and the gradient of conformation increase close to the free surface.

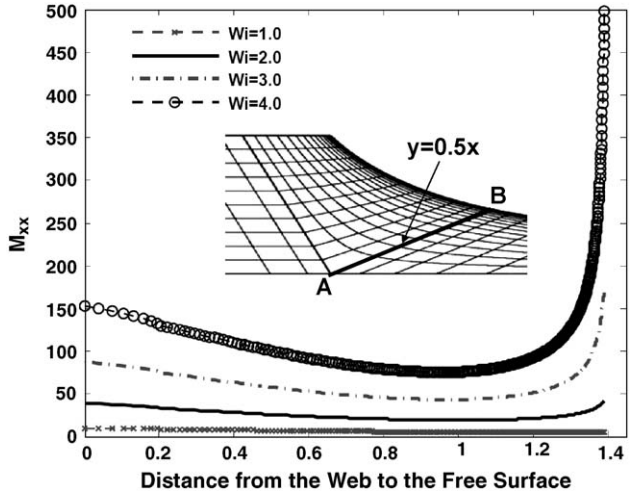

Fig. 4. *xx* component of the conformation tensor for an ultra-dilute solution of Oldroyd-B fluid along line AB ($y = 0.5x$). For an ultra-dilute solution, the position of line AB does not change with Wi and hence, the equation of line AB, $y = 0.5x$, is independent of *Wi*. Computations are carried out using M4 mesh. $Ca = 0.1$, $Q = 0.3$, $\beta = 1.0$.

Mesh refinement is required to capture the conformation layers close the free surface at much higher *Wi*.

It is also observed from Fig. 3 and Table 3 that computations using the FENE-P model remain stable (conformation tensor remains positive definite) to a much higher *Wi* when compared to the Oldroyd-B model for a given mesh refinement. This is consistent with the findings of Pasquali and Scriven [12].

Fig. 5 compares the largest and smallest eigenvalues of the conformation tensor obtained with the micro–macro method and the macroscopic method. The figure clearly indicates that computations using the micro–macro method are stable at much higher *Wi* than those for the macroscopic method. The stability of the micro–macro method can be attributed to the inherent positive definiteness of the conformation tensor. The steady state values reported using the micro–macro approach are a time and ensemble-average over all the Brownian configuration fields after the system reaches a stationary state. The error bars are smaller than the size of the symbols.

Fig. 5 (a) and (b) shows that the results using the micro–macro approach for Hookean dumbbells depart from results using the

Table 3
Maxmium *Wi* achieved in calculations for Oldroyd-B and FENE-P the using macroscopic constitutive equations for ultra-dilute solution, $\beta = 1.0$

Mesh	$Wi^{\max}$ (Oldroyd-B)	$Wi^{\max}$ (FENE-P)
M1	2.68	3.02
M2	3.08	3.66
M3	3.38	5.27
M4	5.45	8.25

Please cite this article as: Mohit Bajaj et al., Multiscale simulation of viscoelastic free surface flows, J. Non-Newtonian Fluid Mech. (2006), doi:10.1016/j.jnnfm.2006.04.009.

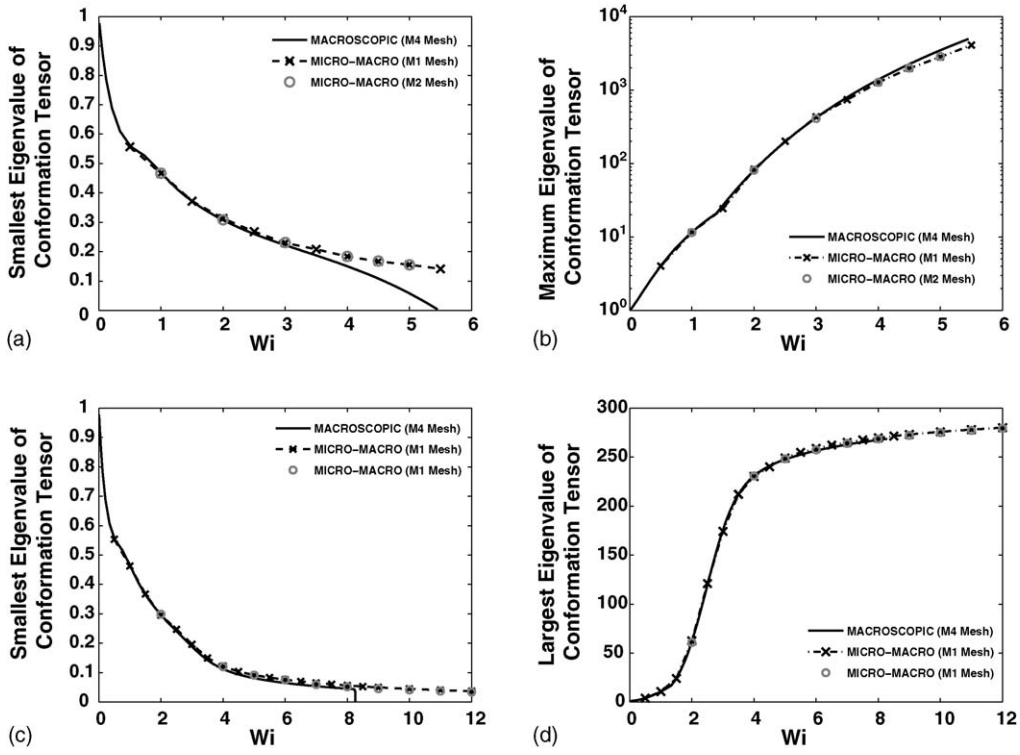

Fig. 5. Comparison of the largest and smallest eigenvalues of the conformation tensor for an ultra-dilute solution obtained from macroscopic and micro–macro approach. Hookean dumbbells [(a) and (b)] and FENE-P dumbbells [(c) and (d)]. $Ca = 0.1$, $Q = 0.3$, $\beta = 1.0$, $b_{\mathbf{M}} = 100$, $N_{\mathrm{f}} = 2000$.

macroscopic approach at $Wi \sim 3$, beyond which the smallest eigenvalues using the macroscopic method drops quickly to zero. However, for all the values of Wi investigated in this work, the conformation tensor computed using the micro–macro method remains positive definite. At higher Wi ($Wi > 5$) it is found that several relaxation times must be computed before a steady state is achieved for the Hookean dumbbell model. The micro–macro simulations of FENE-P dumbbells (see Fig. 5(c) and (d)) show similar qualitative behavior but computations at high $Wi(\sim 12)$ remain numerically stable as the dumbbell reaches its maximum extension.

Fig. 6 examines the time step convergence of the steady state results obtained with the micro–macro method for Hookean dumbbells. It is clear that within statistical error bars the largest eigenvalue of conformation tensor at steady state, for a time step of 0.02 is identical to those obtained for a time step of 0.0075. The eigenvalue for both time steps eventually coincide with the final steady state value obtained using the macroscopic Oldroyd-B model. The steady state value for the higher time step value (0.05) settle down to a lower value than the one obtained using the Oldroyd-B model but it remains within error bars. Error bars in Fig. 5 are smaller than those displayed in Fig. 6 because error bars for steady state averages in Fig. 5 are evaluated by carrying out time and ensemble-averages over all the configuration fields, while error bars for transient averages in Fig. 6 are evaluated only via ensemble average.

Hereafter all reported micro–macro simulations have been carried out with $\Delta t = 0.02$ unless otherwise specified.

Fig. 7 displays the sensitivity of the micro–macro solution to ensemble size. Ensemble sizes of 500, 1000 and 2000 dumbbells are chosen to run simulations for a particular case of $Wi = 2.0$ and $\beta = 1.0$. As expected, the solution gets increasingly more accurate as the ensemble size increases, i.e. the number of dumbbells or the number of trajectories increases. The temporal fluctuations in the largest eigenvalue of the conformation tensor are more pronounced for an ensemble size of 500 than for an ensemble size of 1000 or 2000. Here, an ensemble size of 2000 dumbbells is chosen for all the micro–macro computations in order to have a smaller variance in the field variables.

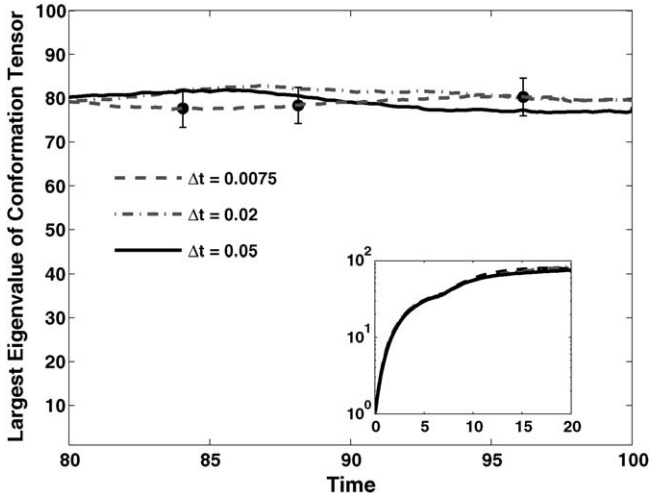

Fig. 6. Time step convergence of micro–macro method for an ultra-dilute solution of Hookean dumbbells. Inset shows the change in the eigenvalue at initial times. $Ca = 0.1$, $Q = 0.3$, $Wi = 2.0$, $\beta = 1.0$, $N_{\mathrm{f}} = 2000$.

Please cite this article as: Mohit Bajaj et al., Multiscale simulation of viscoelastic free surface flows, J. Non-Newtonian Fluid Mech. (2006), doi:10.1016/j.jnnfm.2006.04.009.

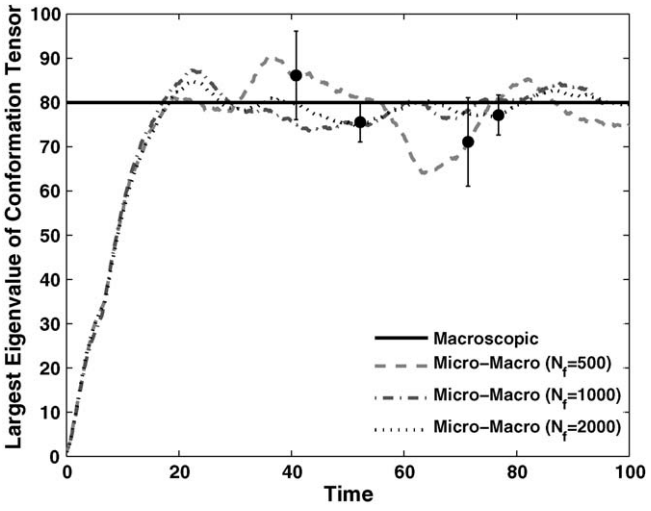

Fig. 7. Effect of the ensemble size (micro–macro approach) on the largest eigenvalue of the conformation tensor for Hookean dumbbells in an ultra-dilute solution. Computations are carried out with the M1 mesh. Error bars are shown for $N_f = 500$ and 2000. $Ca = 0.1$, $Q = 0.3$, $Wi = 2.0$, $\beta = 1.0$, $\Delta t = 0.02$.

The mesh convergence of the evolution of the largest eigenvalue of the conformation tensor for Hookean dumbbells for two different ensemble sizes using the micro–macro approach is shown in Fig. 8. Note that Fig. 5 demonstrates the mesh convergence of the steady state results. It is evident that in order to address the issue of mesh convergence, a sufficiently large ensemble of configuration fields must be chosen. For $N_f = 1000$, the presence of large fluctuations prevents a clear demonstration of mesh convergence. For $N_f = 2000$, mesh convergence is evident.

Fig. 9 shows the components of the conformation tensor M_{xx}, M_{xy} and M_{yy} along the free surface. The results of the micro–macro method compare very well with the macroscopic method.

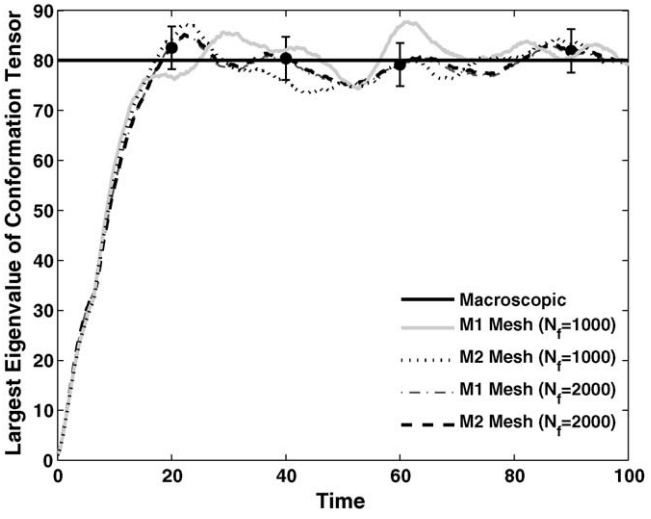

Fig. 8. Mesh convergence of micro–macro approach for Hookean dumbbells for an ultra-dilute solution. Figures shows mesh convergence for two different ensemble sizes. $Ca = 0.1$, $Q = 0.3$, $Wi = 2.0$, $\beta = 1.0$, $\Delta t = 0.02$, $N_f = 2000$.

Table 4
Mesh convergence of calculations for Oldroyd-B and FENE-P using macroscopic constitutive equations for dilute solution, $\beta = 0.75$

Mesh	Wi^{max} (Oldroyd-B)	Wi^{max} (FENE-P)
M1	2.68	2.98
M2	3.31	3.29
M3	3.33	3.30
M4	3.37	3.33

4.1.2. Dilute solution

In dilute solutions the evolution equations of the conformation tensor and of configuration fields are coupled with the mass, momentum and mesh equations. The flow field is computed by solving the coupled set of equations for both the Oldroyd-B and FENE-P constitutive equations using a viscosity ratio $\beta = 0.75$. Fig. 10 shows the largest and smallest eigenvalues of the conformation tensor as a function of *Wi*. It is clear from Fig. 10 that mesh refinement does not increase the maximum *Wi* achieved for dilute solutions as compared to the ultra-dilute solutions (see Fig. 3). The failure of the simulations is neither affected by mesh refinement (i.e. M2, M3 and M4 meshes fails at almost the same *Wi*), nor by changing the molecular model (i.e. the catastrophic failure for Oldroyd-B and FENE-P models occurs at nearly the same *Wi* (as seen in Table 4)). This is in strong contrast to simulations for ultra-dilute solutions. The origin of this behavior may be due to the inappropriate boundary condition applied on the momentum equation at the contact line having a more pronounced effect on the solution of the conformation tensor equation for dilute solutions [23].

Fig. 11, which is further evidence for the numerical stability of micro–macro methods, shows the comparison of the largest and the smallest eigenvalues using microscopic models and their macroscopic equivalent models. Though the micro–macro results are from the coarsest mesh (M1), stability is still obtained. We have not explored the limit of the micro–macro method.

Fig. 12 compares contour plots of the largest and smallest eigenvalues of the conformation tensor with the results for the macroscopic method on mesh M1. Clearly, the results for the micro–macro method agree closely with the macroscopic results for the same mesh.

Fig. 13 reveals the effect of β on the stretch of molecules along the free surface. An increase in the polymer concentration ($\beta < 1$) results in an overall decrease in the stretch of the molecules. A detailed analysis of the effect of β on the stability of slot coating flows will be discussed in future publications. As expected, the Oldroyd-B model predicts higher stretch along the free surface when compared to the FENE-P model. The behavior of the smallest eigenvalue is similar to that of the largest eigenvalue.

Table 5 compares the memory and the CPU time requirements for steady state slot coating flow computations using the macroscopic and micro–macro methods for the Oldroyd-B model. It is evident from Table 5 that the CPU time requirements for the micro–macro approach are much more demanding than the macroscopic approach especially when compared on a single processor and on the same Mesh. However, the micro–macro method can easily be parallelized and the wall time drops significantly after parallelization. Table 5 also compares the memory

Please cite this article as: Mohit Bajaj et al., Multiscale simulation of viscoelastic free surface flows, J. Non-Newtonian Fluid Mech. (2006), doi:10.1016/j.jnnfm.2006.04.009.

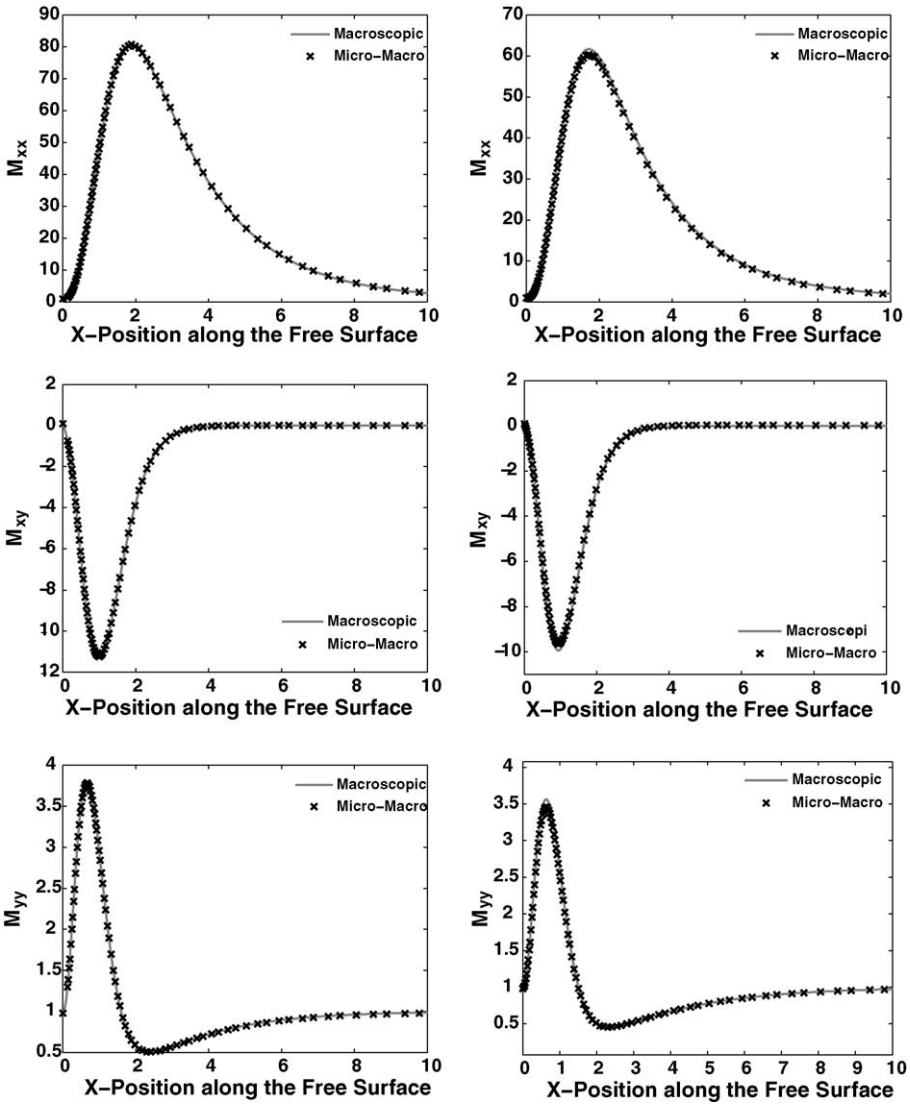

Fig. 9. Comparison of the components of conformation tensor: M_{xx}, M_{xy} and M_{yy} for an ultra-dilute solution. Macroscopic results are for M4 mesh and micro–macro results are for M1 mesh. $Ca = 0.1$, $Q = 0.3$, $Wi = 2.0$, $\beta = 1.0$, $b_{\mathbf{M}} = 100$, $N_{\mathrm{f}} = 2000$. Left: Oldroyd-B; Right: FENE-P.

and the CPU time requirements to solve the BCF equation using the explicit Euler scheme and the proposed fully implicit scheme for the Hookean dumbbell model. Note that explicit computations are done with a time step 0.01, as the explicit scheme is unstable for time step size 0.02. Although the CPU time required for a single time step is the same for both the explicit scheme and the fully implicit scheme, the total CPU time required to reach steady state is much smaller for the implicit scheme as a larger time step can be used while maintaining the same accuracy as the explicit scheme.

It is worth mentioning that the CPU time and memory requirements are independent of the type of microscopic constitutive equation (for a linear dumbbell model) for free surface flow computations using the fully implicit scheme. However, for confined flow problems (fixed mesh), the CPU time required depends upon the type of microscopic constitutive equation used,

Table 5
Comparison of CPU time and memory requirements for the macroscopic and the micro–macro method

Constitutive equation	Number of processors	Time steps	CPU time	Wall time	Memory (MB)
Macroscopic (M1 mesh)	1	Steady state	90 s	90 s	147
Macroscopic (M4 mesh)	1	Steady state	90 min	90 min	2000
Microscopic (Exp. Euler: $\Delta t = 0.02$)	1	Unstable	–	–	−−
Microscopic (Exp. Euler: $\Delta t = 0.01$)	1	1000	32 h	32 h	150
Microscopic (Imp. Euler: $\Delta t = 0.02$)	1	1000	32 h	32 h	150
Microscopic (Imp. Euler: $\Delta t = 0.02$)	8	1000	32 h	4 h	150

$Wi = 2.0$, $\beta = 0.75$, $N_{\mathrm{f}} = 2000$. The micro–macro values are for M1 mesh.

Please cite this article as: Mohit Bajaj et al., Multiscale simulation of viscoelastic free surface flows, J. Non-Newtonian Fluid Mech. (2006), doi:10.1016/j.jnnfm.2006.04.009.

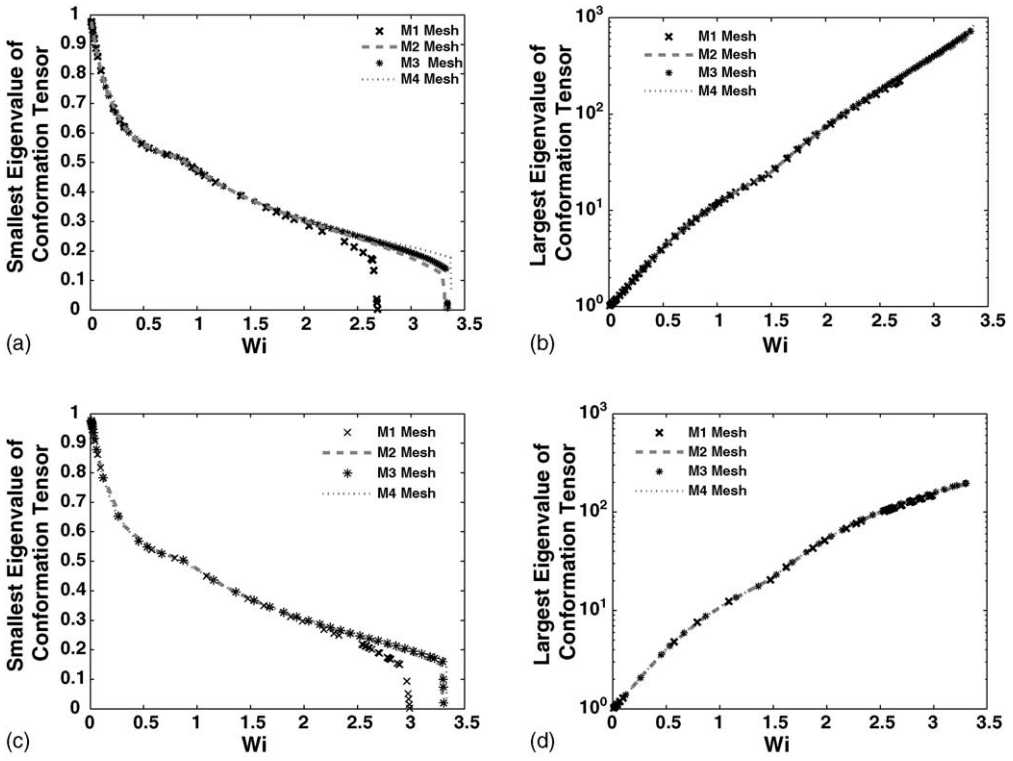

Fig. 10. Largest and smallest eigenvalues of the conformation tensor for an Oldroyd-B liquid [(a) and (b)] and a FENE-P liquid [(c) and (d)]. $Ca = 0.1$, $Q = 0.3$, $\beta = 0.75$, $b_{\mathbf{M}} = 100$. Macroscopic method.

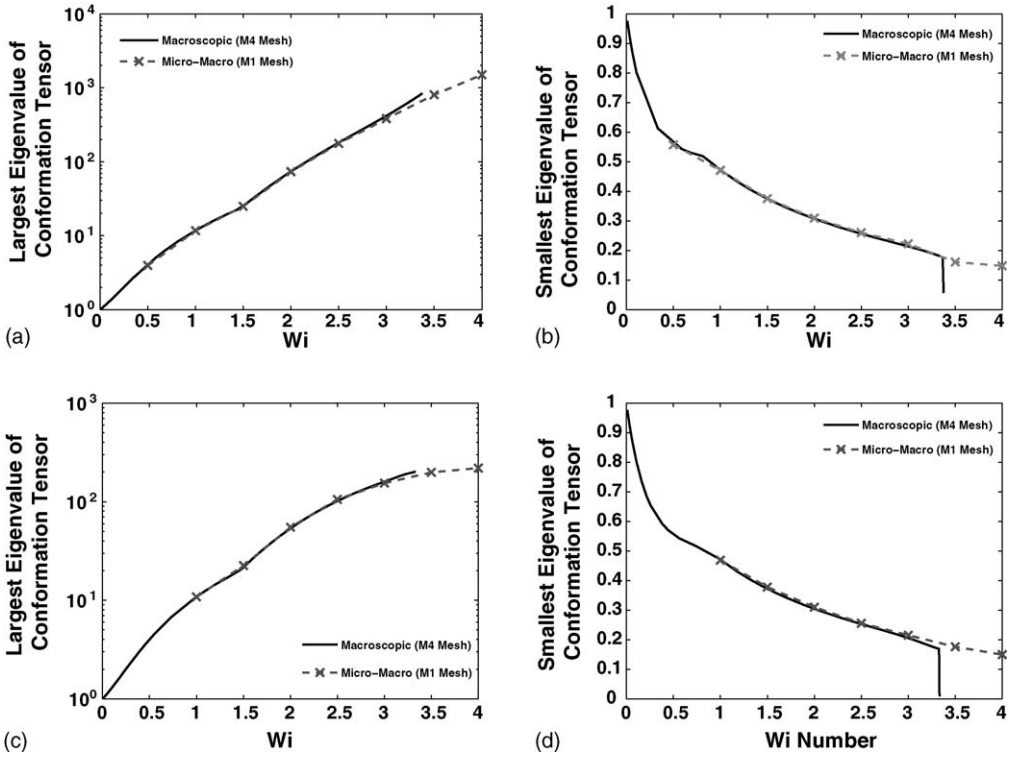

Fig. 11. Comparison of the largest and the smallest eigenvalues of the conformation tensor using the macroscopic and the micro–macro approach. Hookean dumbbells [(a) and (b)] and FENE-P dumbbells [(c) and (d)]. $Ca = 0.1$, $Q = 0.3$, $\beta = 0.75$, $b_{\mathbf{M}} = 100$, $N_{\mathrm{f}} = 2000$.

Please cite this article as: Mohit Bajaj et al., Multiscale simulation of viscoelastic free surface flows, J. Non-Newtonian Fluid Mech. (2006), doi:10.1016/j.jnnfm.2006.04.009.

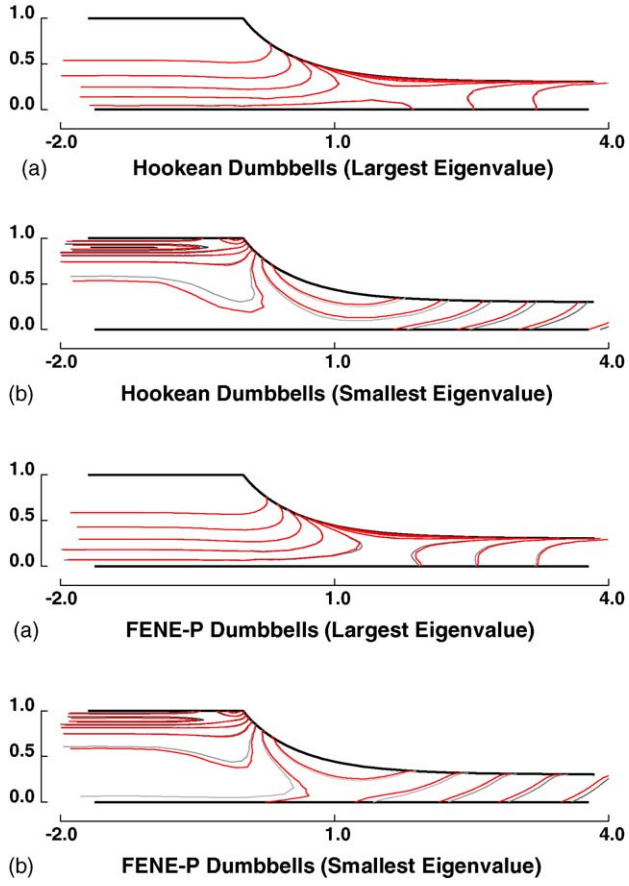

Fig. 12. (Color online) Comparison of contours of the largest (a and c) and smallest (b and d) eigenvalues of the conformation tensor. The macroscopic results are represented by grey lines and the micro–macro results are by red lines. Oldroyd-B [(a) and (b)] and FENE-P [(c) and (d)]. $Ca = 0.1$, $Q = 0.3$, $Wi = 2.0$, $\beta = 0.75$, $b_{\mathbf{M}} = 100$, $N_{\mathrm{f}} = 2000$.

i.e., computations using Hookean dumbbells are less expensive compared to a FENE-P model because the mass matrix [Eq. (33)] is independent of the configurations of the dumbbells and hence it is not required to be factorized at each time step.

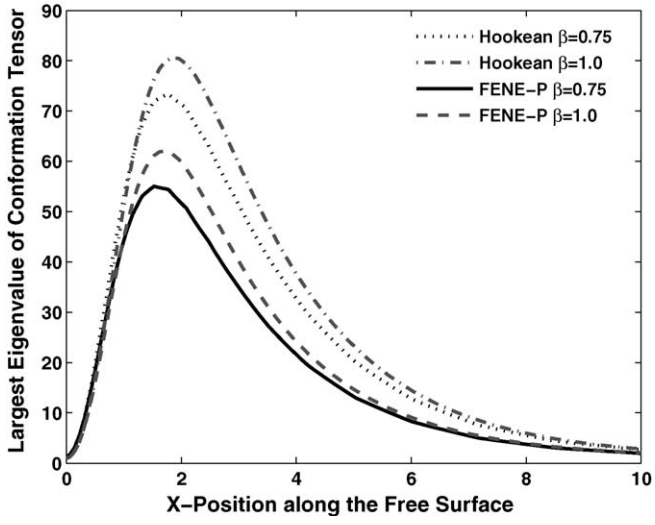

Fig. 13. Effect of viscosity ratio on the stretch of molecules. $Ca = 0.1$, $Q = 0.3$, $Wi = 2.0$, $b_{\mathbf{M}} = 100$.

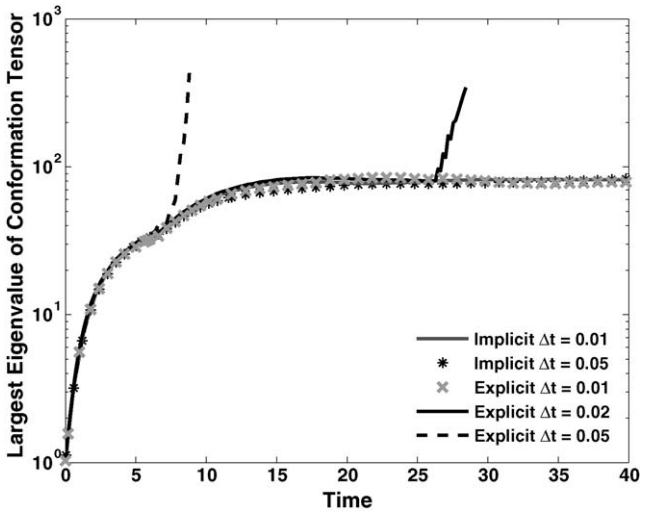

Fig. 14. Comparison of the solution obtained using the explicit Euler scheme and the fully implicit scheme for Hookean dumbbells for $Ca = 0.1$, $Q = 0.3$, $Wi = 2.0$, $\beta = 0.75$, $N_{\mathrm{f}} = 2000$.

Fig. 14 shows the numerical stability of the proposed fully implicit scheme compared to the explicit Euler scheme at $Wi = 2.0$ and $\beta = 0.75$ for three different time steps, namely $\Delta t = 0.01, 0.02$ and 0.05. It is clear that both implicit and explicit schemes are stable for $\Delta t = 0.01$. However, when the time step is increased to 0.02 or 0.05, only the implicit scheme remains stable.

4.2. Non-linear dumbbell models

In this section, we present results using non-linear dumbbell models. Since there are no equivalent constitutive equations for FENE dumbbells and models with hydrodynamic interactions, we only compare results for the non-linear dumbbell models with results of the linear dumbbell models.

Fig. 15 shows the components of the conformation tensor M_{xx}, M_{xy} and M_{yy} along the free surface computed using Newton's method and the collocation method for FENE dumbbells and Hookean dumbbells with hydrodynamic interactions. It is observed that both methods give identical results. The local values of components of the conformation tensor differ by less than 10^{-5} between the two methods.

Fig. 16 displays the ratio of CPU times using the Newton's method and the collocation method as a function of Wi. We observe that collocation method is approximately three times faster than the Newton's method for $Wi < 1.5$ at any given time step. As Wi increases beyond 1.5 the collocation method becomes much more CPU efficient. The CPU time required for the collocation method is relatively insensitive to the values of Wi. However, the CPU time required for the Newton's method increases with increasing Wi since it takes more Newton iterations for the Newton's method to converge. It is also observed in our simulations that for $Wi > 2$, many of the dumbbells are stretched beyond the maximum length $\sqrt{b}$ during the course of Newton's iterations requiring the configuration vectors of these dumbbells to be reset in order to get a physically meaningful spring force law.

Please cite this article as: Mohit Bajaj et al., Multiscale simulation of viscoelastic free surface flows, J. Non-Newtonian Fluid Mech. (2006), doi:10.1016/j.jnnfm.2006.04.009.

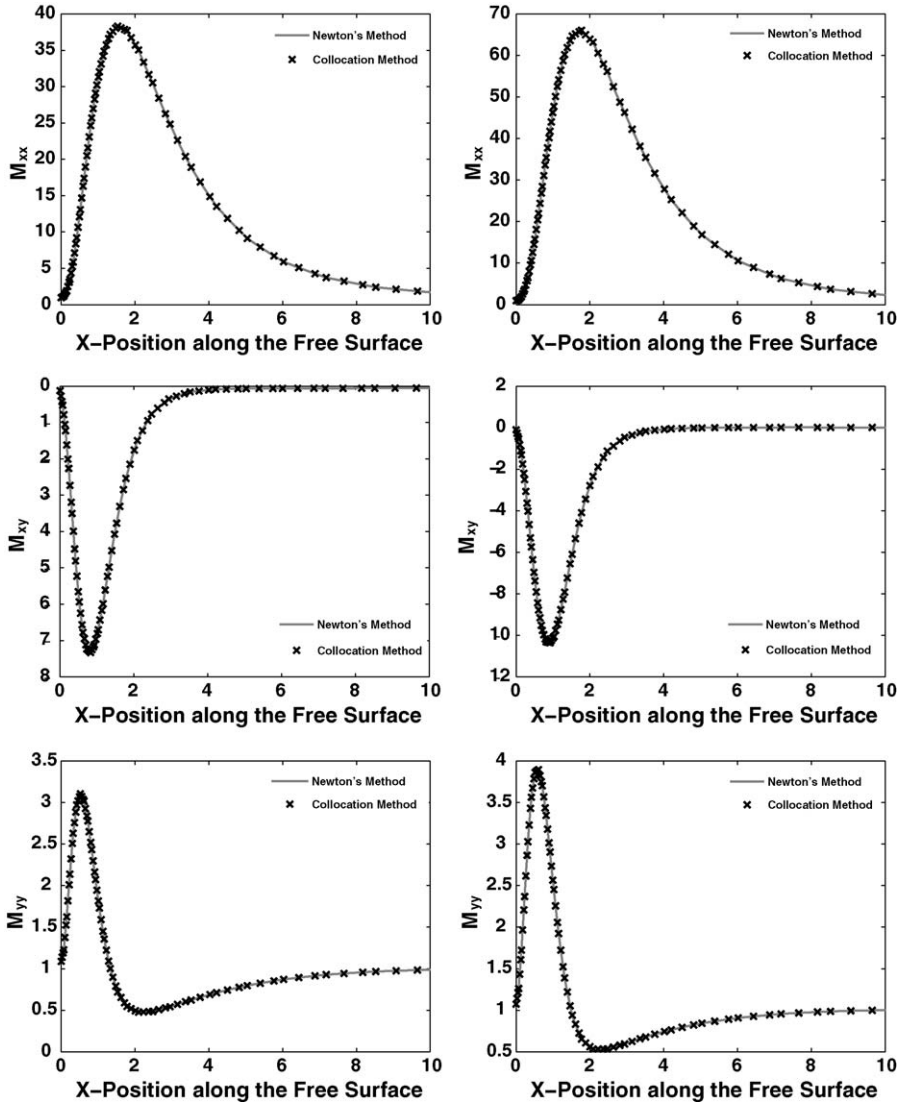

Fig. 15. Comparison of the components of conformation tensor: M_{xx}, M_{xy} and M_{yy} computed using the Newton's method and the collocation method. FENE dumbbells (left) and Hookean dumbbells with HI (right). $Ca = 0.1$, $Q = 0.3$, $Wi = 2$, $\beta = 0.75$, $b_{\mathbf{M}} = 100$, $N_{\mathrm{f}} = 2000$, $h^* = 0.14$.

Table 6 compares the memory and the CPU time requirements for the micro–macro computations using linear and non-linear dumbbell models. The computations for non-linear dumbbell models using the collocation method are almost twice as expensive as computations for linear dumbbell models both in terms of the CPU time and memory requirements. The memory and CPU time required for non-linear dumbbell models are controlled by storage and evaluation of the configuration fields at the predictor step which is not required in the scheme used for linear dumbbell models in this work.

Figs. 17 and 18, which examines the effect of different constitutive models used in this study, show the largest eigenvalue of the dimensionless stress tensor and the stretch of the polymers along the free surface, respectively. The stress, a macroscopic property, appears relatively unaffected by the presence of different non-linear phenomena (except the FENE force). In other words, Hookean dumbbells, Hookean dumbbells with hydrodynamic interactions, and FENE-P dumbbells exhibit nearly same stress along the free surface. On the other hand, the stretch of the polymer, a microscopic property, is significantly different for different constitutive models. The Peterlin approximation to the

Table 6
Comparison of CPU time requirements for linear and non-linear dumbbell models for M1 mesh

Constitutive equation	Number of processors	Time steps	CPU time (h)	Wall time (h)	Memory (MB)
Linear dumbbells	8	1000	32	4	147
Non-linear dumbbells with Newton's method	8	1000	224	28	285
Non-linear dumbbells with collocation method	8	1000	64	8	285

$Wi = 2.0$, $\beta = 0.75$, $\Delta t = 0.02$, $N_{\mathrm{f}} = 2000$.

Please cite this article as: Mohit Bajaj et al., Multiscale simulation of viscoelastic free surface flows, J. Non-Newtonian Fluid Mech. (2006), doi:10.1016/j.jnnfm.2006.04.009.

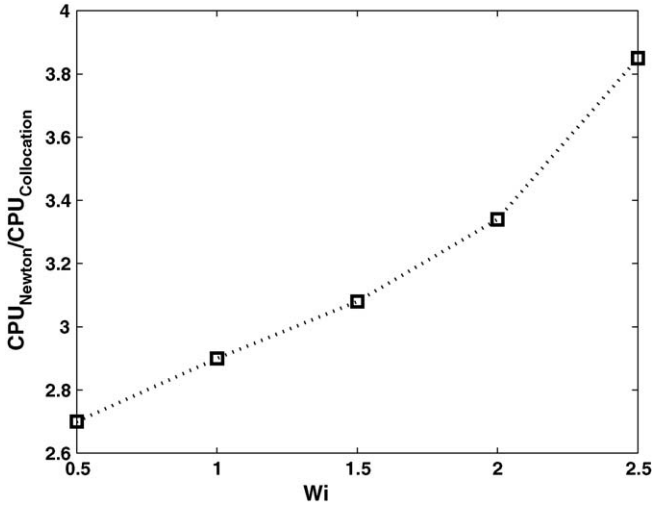

Fig. 16. Comparison of CPU time requirement for the computations of FENE dumbbells using the Newton's method and the collocation method. $Ca = 0.1$, $Q = 0.3$, $\beta = 0.75$, $b_{\mathbf{M}} = 100$, $N_{\mathrm{f}} = 2000$.

FENE dumbbell model over-predicts the stretch. The inclusion of hydrodynamic interactions appears to reduce the stretch in comparison with the pure Hookean dumbbell model.

4.3. Transient results

Here, the evolution of the molecular conformation in the downstream section of a slot coater is studied as the flow evolves from one steady state to another after a gradual change of the dimensionless flow rate from 0.3 to 0.27 at $Wi = 2.0$ and $\beta = 0.75$. The initial condition for all the transient simulations is the steady state solution of flow equations at dimensionless flow rate 0.3, $Wi = 2.0$ and $\beta = 0.75$. The flow rate is gradually changed over a period of 3λ while keeping all other parameters fixed. The gradual change in flow rate ensures a divergence free velocity at

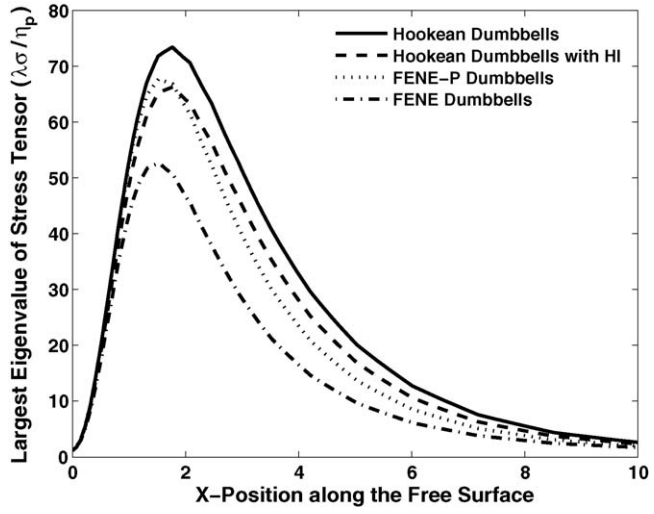

Fig. 17. Largest eigenvalue of dimensionless stress tensor along the free surface for different constitutive models. $Ca = 0.1$, $Q = 0.3$, $b_{\mathbf{M}} = 100$, $\beta = 0.75$, $h^* = 0.14$.

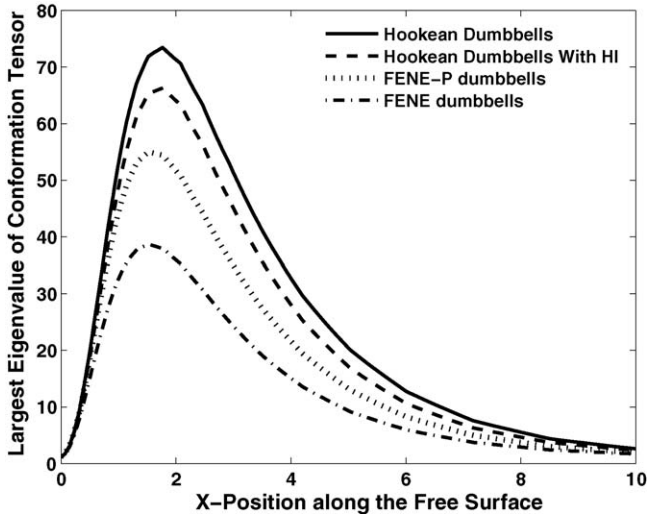

Fig. 18. Stretch (largest eigenvalue of the conformation tensor) of the polymer molecules along the free surface for different constitutive models. $Ca = 0.1$, $Q = 0.3$, $Wi = 2$, $\beta = 0.75$, $b_{\mathbf{M}} = 100$, $N_{\mathrm{f}} = 2000$, $h^* = 0.14$.

each time step which is necessary to calculate the flow field at a subsequent time step [50].

Fig. 19 displays the change in the largest eigenvalue of the conformation tensor by changing the flow rate for an Oldroyd-B fluid and Hookean dumbbell model. Changing the flow rate from 0.30 to 0.27 increases the local velocity gradient under the die lip because the free surface moves inward for a constant web velocity. As a result molecules at a lower flow (0.27) rate are more stretched compared to the those at a higher flow rate (0.30). Transient results calculated using the micro–macro method are subject to statistical fluctuations due to the finite ensemble size of the configuration fields. Fig. 19 shows that by increasing the size of the ensemble from 500 to 2000, the statistical error bar gets smaller as the variance is inversely proportional to the square root of the number of trajectories. The results show

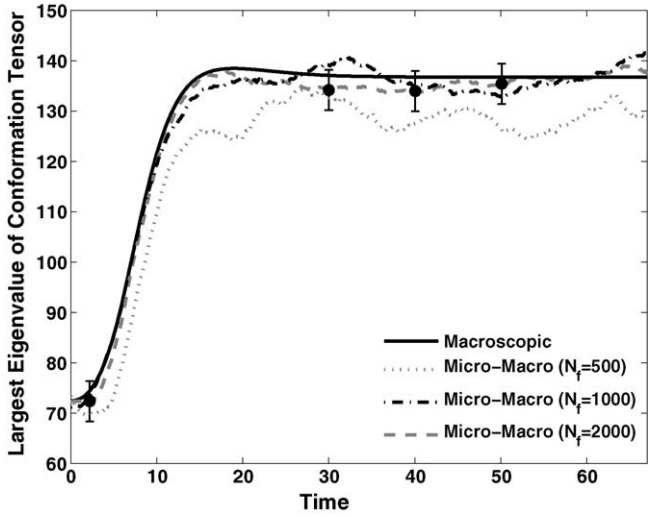

Fig. 19. Change in the largest eigenvalues of the conformation tensor by changing the flow rate for the Hookean dumbbell model. $Ca = 0.1$, $Q = 0.3$, $Wi = 2.0$, $\beta = 0.75$, $N_{\mathrm{f}} = 2000$, $\Delta t = 0.01$. Micro–macro and macroscopic computations are carried out with the M1 and M3 mesh, respectively, and using the fully implicit scheme.

Please cite this article as: Mohit Bajaj et al., Multiscale simulation of viscoelastic free surface flows, J. Non-Newtonian Fluid Mech. (2006), doi:10.1016/j.jnnfm.2006.04.009.

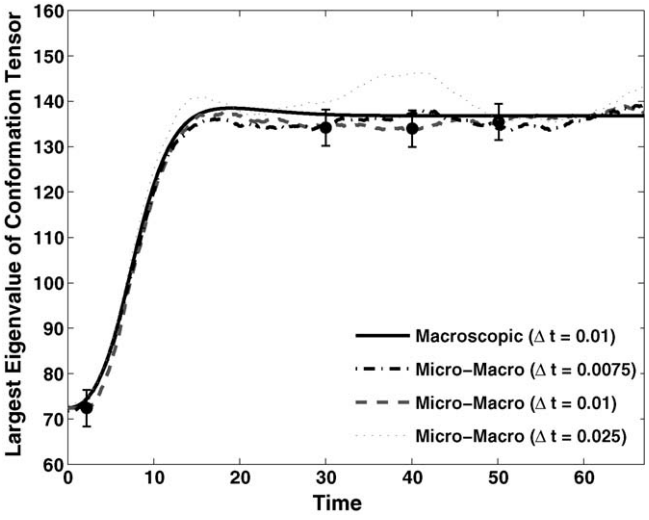

Fig. 20. Time step convergence of the change in the largest eigenvalues of the conformation tensor by changing the flow rate for Hookean dumbbell model. $Ca = 0.1$, $Q = 0.3$, $Wi = 2.0$, $\beta = 0.75$, $N_f = 2000$. Computations are carried out with the M1 mesh and using the fully implicit scheme.

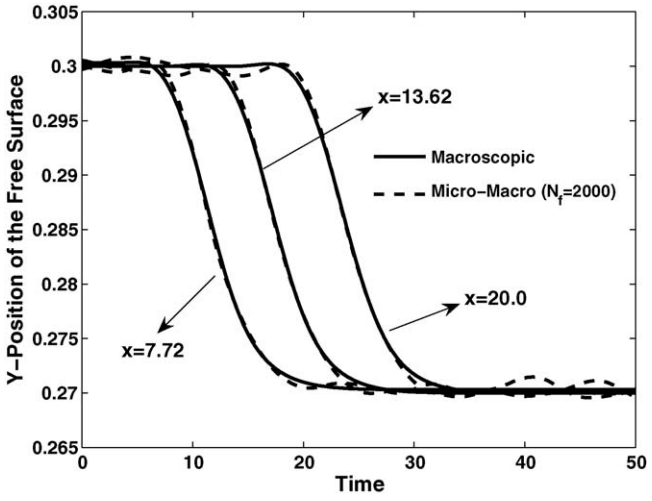

Fig. 22. Change in the Y-position of the free surface at different X-positions along the free surface. Solid lines are for Oldroyd-B model (macroscopic) and dashed lines are for the Hookean dumbbell model (micro–macro). $Ca = 0.1$, $Q = 0.3$, $Wi = 2.0$, $\beta = 0.75$, $\Delta t = 0.01$, $N_f = 2000$. Computations are carried out with the M1 mesh and using the fully implicit scheme.

good comparison between the macroscopic and micro–macro method within statistical error.

Fig. 20 shows the time step convergence of the micro–macro results reported in Fig. 19. It is evident from Fig. 20 that as the time step size gets smaller, the solution gets increasingly more accurate. The results using a time step of $\Delta t = 0.01$ are very close to the results using $\Delta t = 0.0075$. Hence, $\Delta t = 0.01$ is used hereafter.

Fig. 21 shows the change in the coating thickness with time at the outflow plane. It should be noted that although the flow rate is changed at $t = 0$ the coating thickness starts changing only after $t \sim 30$. This in explained in Fig. 22 which shows the change in y-position of the free surface with time at different x-positions along the free surface. As shown in Fig. 22, a front develops at the contact line and propagates downstream like a wave. Figs. 19–22 show that we have a good agreement between the micro–macro and macroscopic methods for transients flows. Transient results for other constitutive models show a behavior similar to that of the Oldroyd-B model.

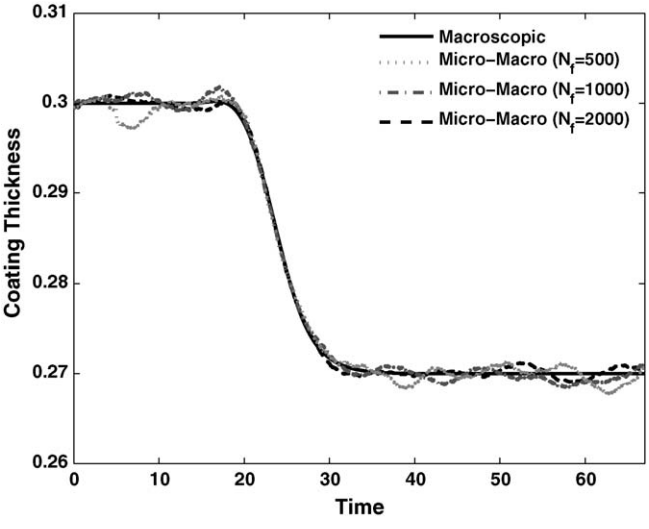

Fig. 21. Change in the coating thickness by changing the flow rate for the Hookean dumbbell model. $Ca = 0.1$, $Q = 0.3$, $Wi = 2.0$, $\beta = 0.75$, $N_f = 2000$, $\Delta t = 0.01$. Computations are carried out with the M1 mesh and using the fully implicit scheme.

5. Conclusion

We have extended the BCF based micro–macro approach to solve transient viscoelastic free surface flow problems. This method involves Brownian dynamics simulation of the motion of polymer molecules coupled together with a time dependent finite element algorithm for the solution of the macroscopic conservation equations. We have validated our method by comparing the flow behavior in the downstream section of a slot coater for linear dumbbell models, i.e., Hookean and FENE-P dumbbells, with their equivalent macroscopic closed form constitutive equations in a conformation tensor based formulation. We found excellent agreement between the results from the BCF approach and the results using the macroscopic approach. An important observation was that the computations using the BCF method were stable at higher Wi and on a relatively coarser mesh when compared to the computations using the macroscopic approach. In addition, a new fully implicit scheme is proposed for the time integration of the BCF equation for linear dumbbell models. We have shown that this scheme is more stable than the explicit Euler scheme with no additional computational and memory requirements for the solution of free surface flows.

We have further extended the capabilities of BCF to solve complex flow problems by using FENE dumbbells and dumbbells with hydrodynamic interactions, for which no closed-form constitutive equations exist. Two different algorithms to solve the non-linear dumbbell models namely, Newton's method and a novel least-squares and collocation method, were examined. We have shown that both algorithms give identical results. How-

Please cite this article as: Mohit Bajaj et al., Multiscale simulation of viscoelastic free surface flows, J. Non-Newtonian Fluid Mech. (2006), doi:10.1016/j.jnnfm.2006.04.009.

ever, the collocation method is fast and computationally efficient when compared to Newton's method. We found significant differences between the stretch of the polymers at the free surface for different microscopic constitutive models.

Acknowledgements

This work has been supported by the Cooperative Research Center for Functional Communication Surfaces, Australia, the National Science Foundation (CTS-CAREER-0124389 and CTS-ITR-0312764) and by gifts from ExxonMobil and 3M Corporation. The authors would like to thank the Australian Partnership for Advanced Computing (APAC) (Canberra, Australia), Victorian Partnership for Advanced Computing (VPAC) (Melbourne, Australia) and the Rice Terascale Cluster funded by NSF under Grant EIA-0216467, Intel, and HP (Rice University, Houston) for the allocation of computing time on their supercomputing facilities. MB and PPB would like to thank Dr. R. Prabhakar, Dr. P. Sunthar, Dr. X. Xueying, Dr. Dhruv Arora and Oscar M. Coronado for useful discussions.

Appendix A. Derivation of the Jacobian matrix for the configuration fields equation

Here, analytical Jacobian entries of the configuration field equation for FENE force are computed. From Eq. (38)

$$\mathbf{G} = \mathbf{Q}_{n+1}\left(1 - \frac{Q^2_{n+1}}{b} + \frac{H\,\Delta t}{\zeta}\right) - \boldsymbol{\Gamma}\left(1 - \frac{Q^2_{n+1}}{b}\right),$$

$$G_i = Q_{i,n+1}\left(1 - \frac{Q^2_{n+1}}{b} + \frac{H\,\Delta t}{\zeta}\right) - \Gamma_i\left(1 - \frac{Q^2_{n+1}}{b}\right),$$

$$G^\alpha_i = \int_\Omega \left[Q_{i,n+1}\left(1 - \frac{Q^2_{n+1}}{b} + \frac{H\,\Delta t}{\zeta}\right) - \Gamma_i\left(1 - \frac{Q^2_{n+1}}{b}\right)\right]\psi^\alpha \,\mathrm{d}\Omega \tag{A.1}$$

The Jacobian entries are obtained by differentiating Eq. (A.1) with respect to $Q^\beta_{j,n+1}$. With $Q_{i,n+1} = Q^\gamma_{i,n+1}\varphi^\gamma_{\mathbf{Q}}$ and $\mathbf{J}^{\alpha\beta}_{ij} = (\partial G^\alpha_i/\partial Q^\beta_{j,\,n+1})$

$$\mathbf{J}^{\alpha\beta}_{ij} = \int_\Omega \left[\left(1 - \frac{Q^2_{n+1}}{b} + \frac{H\,\Delta t}{\zeta}\right)\frac{\partial Q_{i,n+1}}{\partial Q^\beta_{j,n+1}} - \frac{Q_{i,n+1}}{b}\frac{\partial Q^2_{n+1}}{\partial Q^\beta_{j,\,n+1}} + \frac{\Gamma_i}{b}\frac{\partial Q^2_{n+1}}{\partial Q^\beta_{j,\,n+1}}\right]\psi^\alpha \,\mathrm{d}\Omega \tag{A.2}$$

The first derivative on the RHS of Eq. (A.2) is

$$\frac{\partial Q_{i,n+1}}{\partial Q^\beta_{j,n+1}} = \varphi^\gamma_{\mathbf{Q}}\frac{\partial Q^\gamma_{i,n+1}}{\partial Q^\beta_{j,\,n+1}} = \varphi^\gamma_{\mathbf{Q}}\delta^{\gamma\beta}_{ij} = \varphi^\beta_{\mathbf{Q}}\delta_{ij} \tag{A.3}$$

The derivative appearing in second and third term on the RHS of Eq. (A.2) is

$$\begin{aligned}\frac{\partial Q^2_{n+1}}{\partial Q^\beta_{j,n+1}} &= \frac{\partial(\mathbf{Q}_{n+1}\cdot\mathbf{Q}_{n+1})}{\partial Q^\beta_{j,n+1}} = 2\mathbf{Q}_{n+1}\cdot\frac{\partial \mathbf{Q}_{n+1}}{\partial Q^\beta_{j,n+1}}\\ &= 2Q_{k,n+1}\frac{\partial Q_{k,n+1}}{\partial Q^\beta_{j,n+1}} = 2Q_{k,n+1}\varphi^\gamma_{\mathbf{Q}}\frac{\partial Q^\gamma_{k,n+1}}{\partial Q^\beta_{j,\,n+1}}\\ &= 2Q_{k,n+1}\varphi^\gamma_{\mathbf{Q}}\delta^{\gamma\beta}_{kj} = 2Q_{k,n+1}\varphi^\beta_{\mathbf{Q}}\delta_{kj} = 2Q_{j,n+1}\varphi^\beta_{\mathbf{Q}}\end{aligned} \tag{A.4}$$

Combining equations (A.2)–(A.4), we get:

$$\mathbf{J}^{\mathrm{e},\alpha\beta}_{ij} = \int_\Omega \left[\left(1 - \frac{Q^2_{n+1}}{b} + \frac{H\Delta t}{\zeta}\right)\delta_{ij} - \frac{2}{b}Q_{i,n+1}Q_{j,n+1} + \frac{2}{b}\Gamma_i Q_{j,n+1}\right]\psi^\alpha_{\mathbf{Q}}\varphi^\beta_{\mathbf{Q}}\,\mathrm{d}\Omega \tag{A.5}$$

Appendix B. Calculation of characteristic relaxation times and microscopic parameters for different microscopic constitutive models

In this appendix, we discuss the systematic procedure adopted for determining the microscopic parameters H, ζ, h^*, etc., such that identical values for Wi (or equivalently, λ_η) are obtained in all the microscopic constitutive models used in micro–macro computations. The definition of λ_η is

$$\lambda_\eta = \frac{[\eta]^\theta_0 M\eta_\mathrm{s}}{N_\mathrm{A}k_\mathrm{B}T} \tag{B.1}$$

where $[\eta]^\theta_0$ is the intrinsic viscosity in a θ-solution in the limit of zero shear rate, M is the molecular weight and N_A is the Avogadro number. In can be shown for dilute solutions [19,24] that

$$\lambda_\eta = \lim_{n\to 0}\frac{\eta_{\mathrm{p},0}}{nkT} \tag{B.2}$$

The relationship of λ_η to microscopic parameters in models with and without fluctuating hydrodynamic interactions (HI) is discussed separately below. Before we do so, however, the following points are worth noting. In all micro–macro simulations reported here, we set $R^2_\mathrm{e}/3 = 1$ and $k_\mathrm{B}T = 1$, and in models with FENE springs, we choose a value for the FENE parameter $b = 300$. Furthermore, since $\eta_{\mathrm{p},0}$ and λ_η are known for given values of β and Wi, Eq. (B.2) can be used to find the polymer density n in all cases.

(1) *Dumbbells without HI*: For constitutive models without fluctuating HI, the relationship between $R^2_\mathrm{e}/3$ and λ_η, and the microscopic parameters H, b, and $\lambda_H = \zeta/4H$, can be obtained analytically [19,26], and is given in Table B.1. For the fixed values of $R^2_\mathrm{e}/3$, $k_\mathrm{B}T$ and b chosen here, the spring constant H can be evaluated from the expression for $R^2_\mathrm{e}/3$ (see Table B.1). For any particular value of λ_η, the calculated value of H, and the relationship between λ_η and λ_H

Please cite this article as: Mohit Bajaj et al., Multiscale simulation of viscoelastic free surface flows, J. Non-Newtonian Fluid Mech. (2006), doi:10.1016/j.jnnfm.2006.04.009.

Table B.1
End-to-end vector and characteristic relaxation time for different microscopic constitutive models [26]

Constitutive model	$R_e^2/3$	λ_η
Hookean	$k_B T/H$	λ_H
FENE-P	$k_B T(b-3)/Hb$	$\lambda_H(b-3)/b$
FENE	$k_B T(b-5)/Hb$	$\lambda_H(b-5)/b$

(Table B.1), can then be used to determine the value of the drag coefficient ζ to be used in the microscopic model.

(2) *Dumbbells with HI*: The presence of hydrodynamic interactions does not affect static properties, and as a result, expressions for $R_e^2/3$, and the calculation of H, remains unaltered from the cases where HI is absent. However, since λ_η for dumbbells with fluctuating HI cannot be derived analytically, a Green–Kubo formula [56,57] has been used to calculate the shear relaxation modulus $G_p(t)$, from which the characteristic relaxation time can be obtained. Before discussing the Green–Kubo formula below, it is worth noting that in models with HI, rather than the drag coefficient ζ, it is more common to use the non-dimensional parameter h^*. For these models, therefore, the parameter h^* must be chosen such that the desired value of λ_η can be obtained.

The Green–Kubo formula relates $G_p(t)$ to the equilibrium autocorrelation of the quantity $S_{xy} = Q_x\,\partial U/\partial Q_y$ by the expression:

$$G_p(t) = \langle S_{xy}(t) S_{xy}(0)\rangle_{eq} \tag{B.3}$$

It can be shown that λ_η is related to G_p by [26]:

$$\frac{\lambda_\eta}{\lambda_H} = \int_0^\infty G_p(t)\,dt \tag{B.4}$$

For Hookean dumbbells with HI, λ_H is related to h^* by

$$\lambda_H = \frac{3}{2}\left(\frac{\pi}{H}\right)^{3/2}\sqrt{k_B T}\,\eta_s h^* \tag{B.5}$$

Eqs. (B.4) and (B.5) can be combined to give

$$\frac{2\lambda_\eta}{3\,(\pi/H)^{3/2}\sqrt{k_B T}\,\eta_s} = h^* \int_0^\infty G_p(t)\,dt \tag{B.6}$$

The right-hand side of the equation above depends only on h^*, and can be determined once and for all, for any appropriate value of h^*.

Here, the right-hand side is determined by carrying out equilibrium Brownian dynamics simulations. Basically, the product $S_{xy}(t)S_{xy}(0)$ is evaluated after each time step for every equilibrium trajectory, and the average of this product at any time over the ensemble of trajectories gives the autocorrelation function in Eq. (B.3). The values of $G_p(t)$ obtained in this manner are then integrated with respect to t using numerical quadrature. The dependence of the left-hand side of Eq. (B.6) on h^*, determined in this manner, can be plotted as shown in Fig. B.1. For any given value of λ_η and η_s and calculated value of H, the corresponding value of h^* to be used in a microscopic model with fluctuating HI, can consequently be determined from the curve in Fig. B.1.

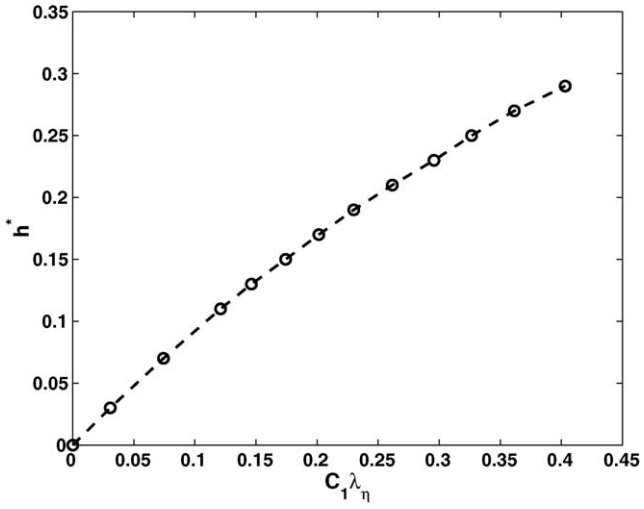

Fig. B.1. Characteristic relaxation time of Hookean dumbbells with hydrodynamic interaction. $C_1 = 2/(3(\pi/H)^{3/2}\sqrt{k_B T}\,\eta_s)$. The line is drawn for guiding the eye. The error bars in the Brownian dynamics simulations are much smaller than the size of the symbols.

References

[1] S.F. Kistler, L.E. Scriven, Coating flow theory by finite element and asymptotic analysis of the Navier–Stokes system, Int. J. Numer. Methods Fluid 4 (1984) 207–229.
[2] K.N. Christodoulou, L.E. Scriven, Discretization of free surface flows and other moving boundary problems, J. Comp. Phys. 99 (1992) 39–55.
[3] P.A. Sackinger, P.R. Schunk, R.R. Rao, A Newton–Raphson pseudo-solid domain mapping technique for free and moving boundary problems: a finite element implementation, J. Comp. Phys. 125 (1996) 83–103.
[4] V.F. de Almeida, Domain deformation mapping: application to variational mesh generation, SIAM J. Sci. Comput. 20 (1999) 1252–1275.
[5] S.F. Kistler, P.M. Schweizer, Liquid Film Coating, Chapman and Hall, New York, 1997.
[6] H. Saito, L.E. Scriven, Study of coating flow by the finite element method, J. Comp. Phys. 42 (1981) 53–76.
[7] W.J. Silliman, L.E. Scriven, Separating flow near a static contact line: Slip at a wall and shape of a free-surface, J. Comp. Phys. 34 (1980) 287–313.
[8] L. Sartor, Slot coating: fluid mechanics and die design, PhD Thesis, University of Minnesota, Minneapolis, MN, 1990 (Available from UMI, Ann Arbor, MI, order number 9109372).
[9] I.D. Gates, Slot coating flows: feasibility, quality, PhD Thesis, University of Minnesota, Minneapolis, MN, 1999 (Available from UMI, Ann Arbor, MI, order number 9946975).
[10] L.C. Musson, Two-layer slot coating, PhD Thesis, University of Minnesota, Minneapolis, MN, 2001 (Available from UMI, Ann Arbor, MI, order number 3008715).
[11] M.S. Carvalho, H.S. Kheshgi, Low-flow limit in slot coating: theory and experiments, AIChE J. 46 (1907–1917) 2000.
[12] M. Pasquali, L.E. Scriven, Free surface flows of polymer solutions with models based on the conformation tensor: computational method and benchmark problems, J. Non-Newtonian Fluid Mech. 108 (2002) 363–409.
[13] A.G. Lee, E.S.G. Shaqfeh, B. Khomami, A study of viscoelastic free surface flows by finite element method: Hele–Shaw and slot coating flows, J. Non-Newtonian Fluid Mech. 108 (2002) 327–362.
[14] G. Bhatara, E.S.G. Shaqfeh, B. Khomami, Influence of viscoelasticity on the interfacial dynamics of air displacing fluid flows—a computational study, J. Non-Newtonian Fluid Mech. 122 (2004) 313–332.
[15] G. Bhatara, E.S.G. Shaqfeh, B. Khomami, The influence of polymer concentration and chain architecture on free surface displacement flows of polymeric fluids, J. Rheol. 49 (2005) 929–962.

Please cite this article as: Mohit Bajaj et al., Multiscale simulation of viscoelastic free surface flows, J. Non-Newtonian Fluid Mech. (2006), doi:10.1016/j.jnnfm.2006.04.009.

[16] O.J. Romero, W.J. Suszynski, L.E. Scriven, M.S. Carvalho, Low-flow limit in slot coating of dilute solutions of high molecular weight polymer, J. Non-Newtonian Fluid Mech. 118 (2004) 137–156.
[17] G.A. Zevallos, M.S. Carvalho, M. Pasquali, Forward roll coating flows of viscoelastic liquids, J. Non-Newtonian Fluid Mech. 130 (2005) 96–109.
[18] M. Bajaj, P.P. Bhat, J.R. Prakash, M. Pasquali, Micro-macro simulation of viscoelastic free surface flows using the Brownian configuration fields method, Proceedings of the 14th International Congress on Rheology, Seoul, South Korea, August 22–27, 2004.
[19] R.A. Bird, R.C. Armstrong, O. Hassager, Dynamics of Polymeric Liquids, vol. 1, 2nd ed., John Wiley & Sons, New York, 1987.
[20] A.N. Beris, B.J. Edwards, Thermodynamics of Flowing Systems with Internal Microstructure, 1st ed., Oxford University Press, Oxford, 1994.
[21] R.J.J. Jongschaap, K.H. de Haas, C.A.J. Damen, A generic matrix representation of configuration tensor rheological models, J. Rheol. 38 (1994) 769–796.
[22] M. Grmela, P.J. Carreau, Conformation tensor rheological models, J. Non-Newtonian Fluid Mech. 23 (1987) 271–294.
[23] T.R. Salamon, D.E. Bornside, R.C. Armstrong, R.A. Brown, Local similarity solutions for the stress field of an Oldroyd-B fluid in the partial-slip/slip flow, Phys. Fluids 9 (1997) 2191–2209.
[24] H.C. Öttinger., Stochastic Processes in Polymeric Fluids, 1st ed., Springer Verlag, Berlin, 1996.
[25] M. Laso, H.C. Ottinger, Calculation of viscoelastic flow using moleculat models: the CONNFFESSIT approach, J. Non Newtonian Fluid Mech. 47 (1993) 1–20.
[26] R.A. Bird, C.F. Curtiss, R.C. Armstrong, O. Hassager, Dynamics of Polymeric Liquids, vol. 2, 2nd ed., John Wiley & Sons, New York, 1987.
[27] K. Feigl, M. Laso, H.C. Öttinger, CONNFFESSIT approach for solving a two-dimensional viscoelastic fluid problem, Macromolecules 28 (1995) 3261–3274.
[28] M. Laso, M. Picasso, H.C. Öttinger, 2-D time-dependent viscoelastic flow calculations using CONNFFESSIT, AIChE J. 43 (1997) 877–892.
[29] M. Laso, J. Ramirez, M. Picasso, Implicit micro–macro methods, J. Non Newtonian Fluid Mech. 122 (2004) 215–226.
[30] J. Cormenz, A. Ledda, M. Laso, Calculation of free surface using CONNFFESSIT, J. Rheol. 45 (2002) 237–258.
[31] E. Grande, M. Laso, M. Picasso, Calculation of variable-topology free surface flows using CONNFFESSIT, J. Non Newtonian Fluid Mech. 1113 (2003) 127–145.
[32] P. Halin, R. Lielens, R. Keunings, V. Legat, The Lagrangian partical method for macroscopic and micro–macro viscoelastic flow computations, J. Non-Newtonian Fluid Mech. 79 (1998) 387–403.
[33] M.A. Hulsen, A.P.G. van Heel, B.H.A.A. van den Brule, Simulation of viscoelastic flow using Brownian configuration fields, J. Non-Newtonian Fluid Mech. 70 (1997) 79–101.
[34] X. Hu, Z. Ding, L.J. Lee, Simulation of 2D transient viscoelastic flow using the CONNFFESSIT approach, J. Non-Newtonian Fluid Mech. 127 (2005) 107–122.
[35] M. Somasi, B. Khomami, Linear stability and dynamics of viscoelastic flows using time-dependent stochastic simulation technique, J. Non-Newtonian Fluid Mech. 93 (2000) 339–362.
[36] M. Grmela, H.C. Öttinger, Dynamics and thermodynamics of complex fluids. I. Development of a general formalism, Phys. Rev. A 56 (1997) 6620–6632.
[37] M. Pasquali, L.E. Scriven, Theoretical modelling of microstructured liquids: a simple thermodynamic approach, J. Non-Newtonian Fluid Mech. 120 (2004) 101–135.
[38] W. Zylka, H.C. Öttinger, A comparison between simulations and various approximations for Hookean dumbbells with hydrodynamic interactions, J. Chem. Phys. 94 (1989) 4628–4636.
[39] J.M. de Santos, Two-phase cocurrent downflow through constricted passages, PhD Thesis, University of Minnesota, Minneapolis, MN, 1991 (Available from UMI, Ann Arbor, MI, order number 9119386).
[40] A. Huerta, W.K. Liu, Viscous flow with large free surface motion, Comp. Methods Appl. Mech. Eng. 69 (1988) 277–324.
[41] R.W. Lewis, S.E. Navti, C. Taylor, A mixed Lagrangian–Eulerian approach to modelling fluid flow during mould filling, Int. J. Numer. Methods Fluids 25 (1997) 931–952.
[42] A. Masud, T.J.R. Hughes, A space-time Galerkin/least-squares finite element formulation of the Navier–Stokes equations for moving domains problems, Comp. Methods Appl. Mech. Eng. 146 (1997) 91–126.
[43] B. Ramaswamy, Numerical simulation of unsteady viscous free surface flow, J. Comp. Phys. 90 (1990) 396–430.
[44] J.C. Slattery, Interfacial Transport Phenomena, Springer-Verlag, 1990.
[45] K.J. Ruschak, Coating flows, J. Fluid Mech. 17 (1985) 65–89.
[46] X. Xie, M. Pasquali, A new, convenient way of imposing open-flow boundary conditions in two- and three-dimensional viscoelastic flows, J. Non-Newtonian Fluid Mech. 122 (2004) 159–176.
[47] R. Guénette, Z. Abdelmalek, A. Fortin, P. Carreau, M. Grmela, Simulation of viscoelastic flows using a conformation tensor model, J. Non-Newtonian Fluid Mech. 45 (1992) 187–208.
[48] R. Guénette, M. Fortin, A new finite element method for computing viscoelastic flows, J. Non-Newtonian Fluid Mech. 60 (1995) 27–52.
[49] A.N. Brooks, T.J.R. Hughes, Streamline Upwind–Petrov–Galerkin formulation for convection dominated flows with particular emphasis on the incompressible Navier–Stokes equations, Comp. Methods Appl. Mech. Eng. 32 (1982) 199–259.
[50] P.M. Gresho, R.R. Lee, R.C. Sani, On the time-dependent solution of the incompressible Navier-Stokes equations in two and three dimensions. In: C. Taylor, K. Morgan (Eds.), Recent Advances in Numerical Methods in Fluids, volume 1, Pineridge Press, Swansea, UK, 1979, p. 27.
[51] M. Luskin, R. Rannacher, On the smoothing property of the Crank–Nicolson scheme, Applicable Anal. 114 (1982) 117–135.
[52] P.P. Bhat, O.A. Basaran, M. Pasquali, Dynamics of viscoelastic liquid filaments: low Capillary number flows. J. Non-Newtonian Fluid Mech (2006)., Submitted to publication.
[53] R. Prabhakar, J.R. Prakash, Multiplicative separation of the influences of excluded volume, hydrodynamic interactions and finite extensibility on the rheological properties of dilute polymer solutions, J. Non-Newtonian Fluid Mech. 116 (2004) 163–182.
[54] M. Somasi, B. Khomami, N.J. Woo, J.S. Hur, E.S.G. Shaqfeh, Brownian dynamics simulation of bead-rod and bead-spring chains: numerical algorithm and coarse-graining issues, J. Non-Newtonian Fluid Mech. 108 (2002) 227–255.
[55] C.C. Hsieh, L. Li, R.G. Larson, Modeling hydrodynamic interaction in Brownian dynamics: simulations of extensional flows of dilute solutions of DNA and polystyrene, J. Non-Newtonian Fluid Mech. 114 (2003) 147–191.
[56] F.G. Diaz, J.G. De la Torre, J.J. Freire, Viscoelastic properties of simple flexible and semirigid models from Brownian dynamics simulations, Macromolecules 23 (1990) 3144–3149.
[57] M. Doi, S.F. Edwards, The Theory of Polymer Dynamics, 1st ed., Oxford University Press, Oxford, 1986.

Please cite this article as: Mohit Bajaj et al., Multiscale simulation of viscoelastic free surface flows, J. Non-Newtonian Fluid Mech. (2006), doi:10.1016/j.jnnfm.2006.04.009.